PHYSICAL REVIEW E VOLUME 57, NUMBER 1 JANUARY 1998

Structure and dynamics of electrorheological fluids

James E. Martin and Judy Odinek
Advanced Materials Physics Division, Sandia National Laboratories, Albuquerque, New Mexico 87185-1421

Thomas C. Halsey
Exxon Research and Engineering, Route 22 East, Annandale, New Jersey 08801

Randall Kamien
Department of Physics, University of Pennsylvania, Philadelphia, Pennsylvania 19104

(Received 14 June 1996; revised manuscript received 26 December 1996)

We have used two-dimensional light scattering to study the structure and dynamics of a single-scattering electrorheological fluid in the quiescent state and in steady and oscillatory shear. Studies of the quiescent fluid show that particle columns grow in two stages. Particles first chain along the electric field, causing scattering lobes to appear orthogonal to the field, and then aggregate into columns, causing the scattering lobes to move to smaller angles. Column formation can be understood in terms of a thermal coarsening model we present, whereas the early-time scattering in the direction parallel to the field can be compared to the theory of line liquids. In simple shear the scattering lobes are inclined in the direction of fluid vorticity, in detailed agreement with the independent droplet model of the shear thinning viscosity. In oscillatory shear the orientation of the scattering lobes varies nonsinusoidally. This nonlinear dynamics is described by a kinetic chain model, which provides a theory of the nonlinear shear rheology in arbitrary shear flows. [S1063-651X(97)10112-X]

PACS number(s): 47.50.+d

I. INTRODUCTION

Electrorheological (ER) fluids [1,2] are made by suspending particles in a liquid whose dielectric constant or conductivity [3–5] is mismatched in order to create dipolar particle interactions in the presence of an ac or a dc electric field. ER fluids rapidly solidify, or at least increase their viscosity dramatically, in response to an electric field, due to the formation of particle chains that bridge the electrodes. The millisecond response of ER fluids has piqued the interest of engineers, who are now trying to incorporate these fluids into practical fast electromechanical actuators, such as fiber spinning clutches and active shock absorbers.

To predict the behavior of ER fluid-based devices a designer must have a good understanding of the both the solidification kinetics and the response of the activated fluid to mechanical stress, especially when flow is induced. We have previously reported preliminary light-scattering studies of the evolution of structure in a quiescent fluid [6], the steady-state structures that form in shear [7], and the nonlinear dynamics of chain structures in oscillatory shear [8]. In this paper we extend those investigations and give a complete account of the light-scattering studies we have made as well as the theoretical ideas that can be invoked to understand the data.

The first experiments we report concern the evolution of structure after an electric field is applied to a quiescent ER fluid. This occurs in two principal phases: the fast aggregation of particles into chains, which occurs in milliseconds, and the slow coalescence of chains into columns, which occurs in minutes. Chain formation has been studied by time-resolved studies of the transmission of light through an opaque ER fluid [9], birefringence and dichroism [10], and fluid permittivity [11]. The light-scattering measurements we report compliment these measurements since they allow determination of the slow column formation as well.

In the Halsey-Toor theory of column formation [12] it is shown that after particle chains form and span the electrodes, the long-range dipolar interactions between vicinal chains are screened by the image dipoles created by the conducting electrodes and the chains then interact via a short-ranged potential that arises from one-dimensional Landau-Peierls charge-density fluctuations. The chains then coalesce in the plane orthogonal to the field to form a three-dimensional solid [13]. Our measurements of the power-law growth of columns as a function of applied voltage and fluid concentration support this general description of coarsening, but the observed voltage dependence has led to the consideration of the case wherein column coalescence occurs before a charge-density fluctuation can relax.

The anisotropic ‘‘bow tie’’ light-scattering pattern we observe is similar in appearance to that predicted by the theory of line liquids. By analyzing our data in ways suggested by this theory we show that there is a strong correspondence of the predictions of line liquid theory to scattering data taken shortly after the quench.

For completeness we mention that within the columns the colloids eventually form a crystalline solid [13] that recent calculations show is body-centered tetragonal [14]. This bct structure has been observed in a laser diffraction experiment from a column of large silica spheres [15]. Of course, a glassy structure may result from a rapid, deep quench.

When an initially quiescent ER fluid is subjected to steady or oscillatory shear, the electrode-spanning columns break into volatile structures that continuously fragment and aggregate, and generally tilt away from strict field alignment in the direction of fluid vorticity. There are two fundamentally different theoretical models of structure and rheology in shear:

1063-651X/98/57(1)/756(20)/$15.00

© 1998 The American Physical Society

the *equilibrium droplet model* [16] and the *kinetic chain model* [17]. In both of these models we use the point dipole approximation, which is reasonably accurate for our colloidal silica fluid, which has negative dielectric contrast. In the droplet model, which was developed for stationary shear, a free energy is minimized in order to compute the equilibrium size, shape, and orientation of particle structures that are presumed to be ellipsoidal. In the kinetic chain model, which can be applied to both stationary and non-stationary shear, a mechanical stability condition determines the metastable size and orientation of structures that are presumed to be chains. The predictions of these models are contrasted as we compare them to our light-scattering data.

Light-scattering measurements in steady shear [7] show how the steady-state size and orientation of these particle structures depends on the shear rate, with the size decreasing and the tilt angle increasing as the shear rate increases. These changes are responsible for the shear thinning of the viscosity of ER fluids [16]. We have extended these measurements to include the voltage dependence.

We report light-scattering studies of the structural dynamics in oscillatory shear flow. These measurements should be of special interest to those interested in modeling the fluid stress response to nonstationary shear flows. Direct rheological studies [18,19] have been complicated by the difficulty in finding a linear-response regime. It has been shown that if a strict linear viscoelastic regime exists at all, it is confined to strain amplitudes smaller than 10^{-2}. Thus the framework of linear viscoelasticity, a phase-shifted stress in response to an applied strain, is of limited utility for ER fluids. Powell [20] has presented rheological data that demonstrate the nonlinear nature of the stress response and these agree quite well with the light-scattering data we present here.

In our measurements of the orientation dynamics in oscillatory shear we find a quasilinear response regime at small strain amplitudes and are able to determine experimental conditions where the droplet orientation is in or out of phase with the strain. This quasilinear regime is successfully described by the independent droplet model, wherein the droplet size does not change during a shear cycle. However, at strain amplitudes larger than about 0.25, chain volatility during a single strain cycle becomes significant and the orientation dynamics becomes strongly nonlinear. In this regime the kinetic chain model gives a very reasonable description of the observed dynamics and agrees well with direct rheological measurements [20] of the stress.

II. EXPERIMENT

A. Sample preparation

The sample used in this study is a model ER fluid we developed for light scattering [6], microscopy, and electrorheological measurements [16]. The colloids in our model fluid are synthesized by the base-catalyzed nucleation and growth of monodisperse silica spheres from tetraethoxysilicon (TEOS). To reduce the Keesom interactions that lead to aggregation, this synthesis was conducted in a mixed organic solvent that index matches the growing spheres. Specifically, to prepare a 200-ml solution we combine 21.2 ml of 29.5-wt. % NH_3 with 39.2 ml of formamide, 117.2 ml of benzyl alcohol, and 22.4 ml TEOS. The solution is mixed but not shaken and allowed to react without stirring for 2 h. The hydrophilic silica spheres are then coated with 5.0 ml of the organophilic silane coupling agent 3-(trimethoxysilyl) propyl methacrylate via a condensation reaction [21]. After a 24-h vacuum distillation of water and ammonia at 50 °C the spheres are centrifuged at low acceleration (~ 35 g for 7 h, the supernatant decanted, and the soft colloidal solid is redispersed in 4-methylcyclohexanol, again chosen to closely index match the spheres. The sample is centrifuged again at 35 g for 16 h, the supernatant decanted, and the solid resuspended in 4-methylcyclohexanol. To prevent settling the final sample is rotated slowly until used.

Scanning electron microscopy and elastic and quasielastic light-scattering measurements indicate that 0.7-μm-diam silica spheres are easily formed at high silica concentrations under mild hydrolysis with 0.5 M NH_4OH. The elastic light-scattering data are consistent with a Gaussian sphere radius R distribution having σ_R/R of 10.5%. Light-scattering intensity measurements indicate a refractive index increment of $dn/dc = 0.0017$ ml/g, which is small enough to ensure single scattering from concentrated dispersions: Indeed, depolarization of the scattered light was negligible.

To measure the surface charge of the colloids, electrophoresis measurements were made in a Pen Kem Laser Zee microelectrophoresis apparatus. Since we were unable to observe any electrophoresis with this apparatus we simply applied a 1-kV/mm electric field to the particles and observed their behavior through a Nikon Microphot-FXA optical microscope. Even at these high electric fields we were unable to observe electrophoresis of these particles, although at high applied frequencies field-induced particle chaining was observed and found to be reversible by Brownian motion alone, indicating that contact interactions between these particles are much smaller than k_BT.

The two samples used in the study measured 20 and 34 wt. % by thermal gravimetric analysis, although the high-concentration sample was diluted to 11 wt. % for the kinetics studies. The fluid used in the oscillatory shear study is 7.5-wt. % silica, which is 3.0 vol %, assuming a silica specific gravity of 2.5. This corresponds to a mean separation between silica sphere centers of $\sim 6R$ and a spacing of $\sim 11R$ between initially formed chains.

B. Two-dimensional light scattering

To study the kinetics of phase separation requires the ability to determine structure as a function of time. Traditional one-dimensional light-scattering instruments must repetitively scan through a sequence of angles, with the result that data are acquired in an interval during which the structure is evolving, so that temporal resolution is severely compromised. Furthermore, the ER phase transition gives rise to anisotropic scattering and therefore a two-dimensional detector is required. To meet these demands we have developed a light-scattering instrument that is based on readily available video and computer technology.

A 454.5-nm argon-ion laser beam, focused with a 40-cm focal length lens, illuminates the sample, the scattered light impinges on an opaque diffusing screen, is collected by a fixed-gain Pulnix video camera, and is stored on a video cassette recorder at a spatial resolution of 640×480. The video frames are then grabbed from the tape and eight-bit digitized by a Perceptics PixelBuffer card on a Macintosh Quadra 950. The frame grabber card immediately transfers these images to a 32-Mbyte dual-ported PixelStore memory board that resides on both the slow computer bus and a very fast direct bus from the frame grabber that can support the data transfer rate of 10 Mbyte/s. The digitized images have a dynamic range of 256, a spatial resolution of 512×480, and a temporal resolution of $\frac{1}{30}$ s.

The length scale regime that can be studied with 454.5-nm light is from $2\pi/q=22$ to 0.95 μm, where $q=4\pi\sin(\theta/2)/\lambda$ is the scattering wave vector, θ is the scattering angle, and λ is the wavelength in the scattering medium.

The scattered light that ultimately arrives at the charge coupled device array is not the true scattered intensity that emerges from the scattering volume. In fact, the measured scattered intensity increasingly underestimates the true intensity as the scattering angle increases. The loss of scattered light is due to a number of causes and although each of these is small, they combine to give a correction factor of almost two at the highest measured wave vector, relative to zero angle. We correct for the incident polarization of the laser, the polarization and incident-angle-dependent cell and scattering screen reflectances, the angular distribution of the emerging light from the diffusing screen, camera vignetting, the Jacobian for light refraction, and the Jacobian of the projection of a sphere onto a flat screen (twice).

We calculate each of these corrections analytically and apply these to a 512×480 constant intensity image to create a 512×480 ''template.'' Each scattering image was then corrected by multiplying by the template on a pixel-by-pixel basis. Calibration runs with a uniform scatterer yielded an essentially constant scattering image after these corrections were applied, with only a small drop in the intensity at high q.

C. Scattering cells

The scattering cell for the quiescent fluid studies consists of a black nylatron body with a cylindrical cavity into which 1.0-mm-diam black anodized cylindrical aluminum electrodes were threaded. Flat glass microscope slides were pressed against rubber O rings to provide a seal. A 12.0-kHz sine wave was applied to the 0.72-mm electrode gap to induce particle chaining.

The scattering cell for the shear studies consists of an inner (40×2)-mm flat circular electrode that is concentric to a 42-mm hole in an outer electrode, creating a radial electric field in a 1.0-mm gap. The outer electrode is sandwiched between plastic and both electrodes are embedded between glass plates, with a fluid-filled 2.0-mm gap between the inner circular electrode and each glass plate. The radial electric field is parallel to the shear gradient in the fluid.

For the steady shear studies a dc servo motor was used to drive a pulley on the inner electrode. In the oscillatory shear studies the inner electrode was caused to oscillate sinusoidally by a long rod connected to a 25-mm lever on the electrode shaft, which is driven open loop by an adjustable eccentric shaft on a powerful 300-oz-in. microstepping motor. The strain amplitude can be varied by adjusting the eccentric and the strain frequency can be varied by adjusting the microstepping controller speed. The detector response time limits the maximum frequency to ~1 Hz.

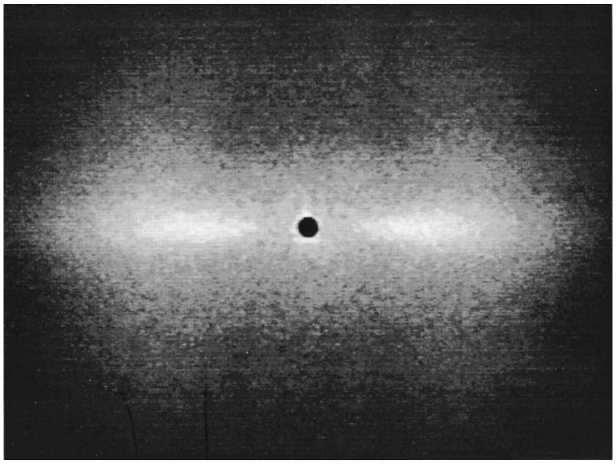

FIG. 1. Within milliseconds of an electric-field quench into the two-phase region the scattered intensity from an electrorheological fluid shows two distinct lobes (the maximum scattering angle is ~8° here). These lobes, which are orthogonal to the electric field, indicate the presence of an unstable concentration fluctuation that is due to column formation. This scattering pattern is the two-dimensional analog of the ''spinodal ring'' commonly observed in the first-order phase separation of three-dimensional systems.

The electric field is supplied by a square wave from a Trek power supply driven by Wavetek signal generator. Voltages are reported peak to peak. The dielectric constant of 4-methylcyclohexanol is 13.5 and silica is ~4.

D. Strain phase determination

One problem in this experiment is the phasing of the applied strain with the scattering data. To solve this problem, we devoted a small corner of the scattering screen to an optical ''strain phase clock.'' This clock was created by running a second pulley, whose rotational axis is orthogonal to the scattering screen, synchronously with the stepping motor. Inside this second pulley is mounted a prism that deflects by several degrees a He-Ne laser beam directed toward the scattering screen. As the pulley turns, the laser beam scribes a small circle on the scattering screen. The strain phase clock can be set by means of a rotational adjustment of the prism. Each image thus contains both the scattering data and the absolute strain phase.

III. QUIESCENT FLUID

The first measurements we report concern the growth and structure of the fluid in the quiescent state. Preliminary measurements of the structure orthogonal to the field were reported earlier [6], here we extend those results and present an analysis of the structure parallel to the field.

A. Domain structure orthogonal to the field

Scattering data taken shortly after an electric-field quench, shown in Fig. 1, demonstrate an unstable concentration fluctuation orthogonal to the electric-field lines in the fluid. The two scattering lobes have an intensity maximum at some

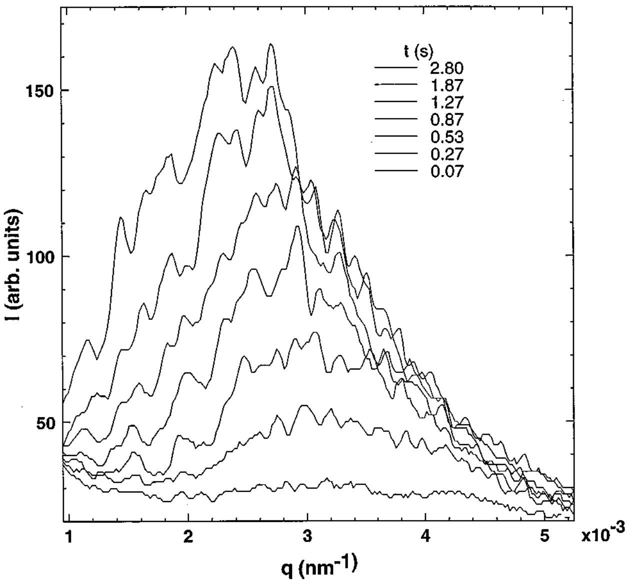

FIG. 2. Intensity slices through the lobes, i.e., orthogonal to the electric field, indicate that the peak intensity increases with time and moves to larger length scales (smaller q). The scattering functions are noisy because fluctuations are slow; the number of particles in the scattering volume is small.

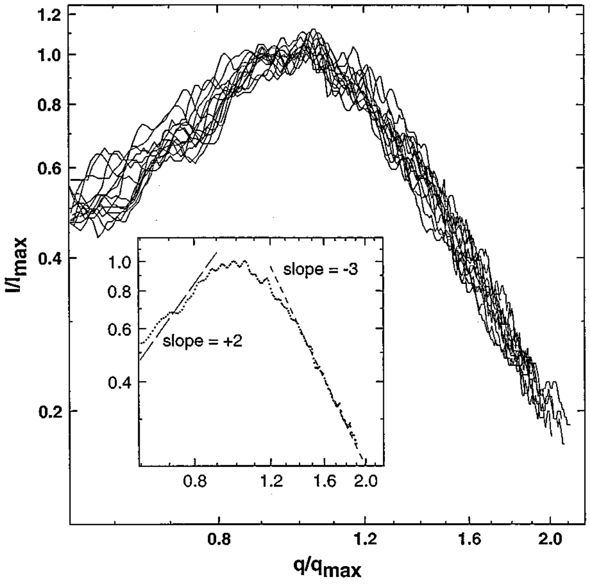

FIG. 3. A master curve is obtained when the scattered intensity data are plotted on dimensionless axes, indicating scaling of the domains. Averaging these data results in the inset scattering curve, which demonstrates a q^{-3} fall off the data on the high-q side of the peak. This falloff, which is Porod's law for a two-dimensional system, indicates sharp nonfractal interfaces on the columns. The scattering function on the low-q side of the peak increase as q^{-2}. This is expected for spinodal decomposition and is a consequence of a conservation law.

nonzero wave vector, indicating strong spatial correlations between initially formed chains in the plane orthogonal to the field. The scattering patterns fades when the field is turned off, indicating the reversibility of particle chaining. (The Bragg scattering one would expect from chains of regularly spaced particles is at values of q larger than observable with our instrument, but can be seen on the image screen.) Reversible chaining is also observed in direct optical imaging.

The distinctive scattering lobes are superficially the two-dimensional counterpart to the spinodal ring observed in three-dimensional systems and thus compel a comparison to this model. In fact, if the laser beam is directed along the field lines, by using transparent electrodes, a scattering ring can be observed. We will show that more information can be obtained in our scattering geometry.

The time evolution of the structure factor can be analyzed by taking a slice through a lobe in the direction orthogonal to the electric field lines, as shown in Fig. 2. Each of these single video frames is intrinsically noisy because the number of chains in the scattering volume is small, but it is nonetheless clear that the scattered light increases in intensity and the peak position moves to smaller q as time evolves.

An elementary question is whether or not the domain structures scale, i.e., merely enlarge with time while maintaining the same morphology. In a scattering experiment two fundamental quantities are obtained: a characteristic domain length L and the domain mass within a volume of size L^d, where d is the spatial dimension. In our case the characteristic length can be identified with the inverse peak position $L(t)=2\pi/q_{\max}(t)$ and the characteristic mass is the peak intensity $I_{\max}$. The collapse obtained by plotting the scattering data against axes normalized by these quantities (Fig. 3) demonstrates that the domains scale.

We can analyze the data further to understand the structure of the domains. For example, if the aggregating chains stick upon contact, without rearranging to minimize their electrostatic energy, then one might expect mass fractal, two-dimensional cluster-cluster aggregation to describe the structure of a cross section of a column. It is also possible that sheetlike cross sections evolve or even surface fractals. In fact, the scaled and averaged scattering data (inset in Fig. 3) have a high-q shoulder that decays as q^{-3}, which is *Porod's law* for two dimensions. Porod's law indicates the presence of sharp nonfractal interfaces, as expected for a system that is spinodally decomposing. By comparison, mass fractal scattering would yield a high-q decay that is slower than q^{-2} for a two-dimensional system.

It is also possible to test for the formation of fractal domains by the relationship of the characteristic mass and length. The data in Fig. 4 demonstrate that $I_{\max}\sim q_{\max}^{-2.25}$, suggesting that within experimental error the standard scaling relation for spinodal decomposition

$$I(t)\sim q_{\max}^{-d}(t)f(q/q_{\max}(t)), \tag{1}$$

$$f(x)\sim x^{-d-1} \quad \text{for } x\gg 1$$

applies since $d=2$. However, this result is simply a consequence of the growth of nonfractal domains that have a size-independent morphology and so is more general than spinodal decomposition.

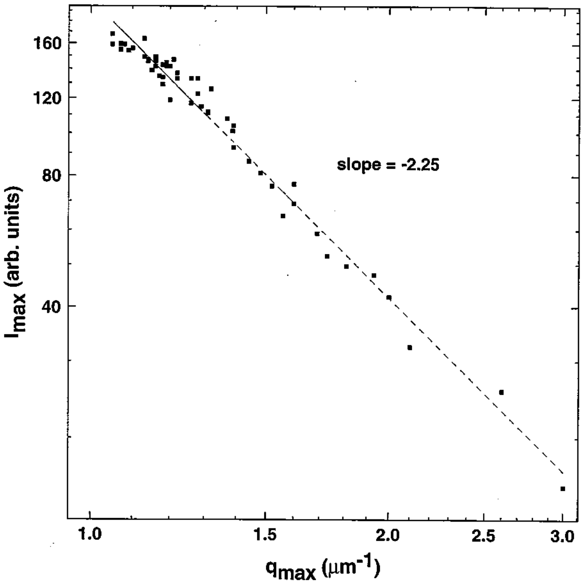

FIG. 4. The peak intensity $I_{\max}$ scales with the peak position as $I_{\max} \sim q_{\max}^{-2.25}$. Within the errors of this experiment this indicates that the scaling relation $I_{\max} \sim q_{\max}^{-d}$ is obeyed since the dimension d of this system is 2.

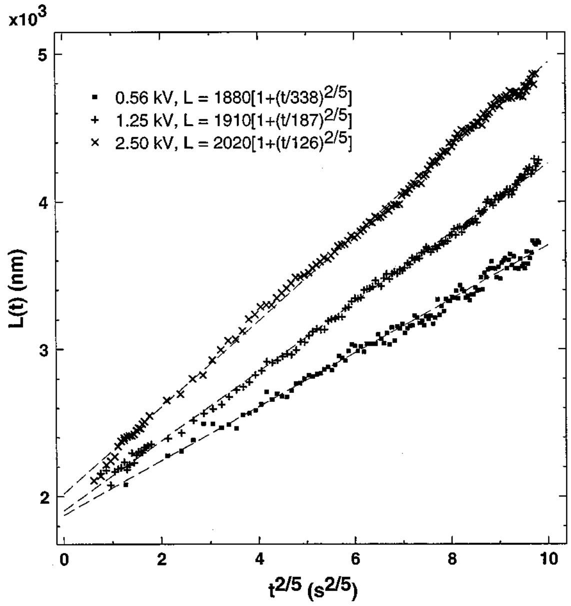

FIG. 5. The kinetics of structural coarsening is well described by the power law $L(t)=L(0)[1+(t/\tau)^{2/5}]$, where $L(t)=2\pi/q_{\max}$ is the characteristic length. For spinodal decomposition in a system with a conserved order parameter one expects $L(t) \sim t^{1/3}$. An important conclusion of these experiments is that the rate of coarsening is voltage dependent, as quantified in the inset.

B. Domain growth

Experimental studies of the domain growth kinetics were complicated by the intrinsically noisy scattering signal, which led to unacceptable errors in judging the peak position and intensity from the scattering data. To reduce the noise in the characteristic length $L(t)=2\pi/q_{\max}(t)$ we computed the moments

$$I_k(q_l,q_u) \equiv \int_{q_l}^{q_u} q^k I(q)\, dq. \tag{2}$$

This integral converges only for $k<2$, so we used the zeroth and first moments. In our experiment the lower integration limit $q_l = 0.33 \times 10^{-3}$ nm^{-1} is determined by the beam stop radius and the upper limit $q_u = 0.529 \times 10^{-2}$ nm^{-1} is set by the camera position. These experimentally fixed integration limits cause truncation errors in the determination of the moments, a point that deserves some consideration.

Truncation errors are of no consequence in determining the functional form of the growth kinetics, provided that the relative error is independent of the domain size. For example, the moments can be determined self-consistently by taking advantage of the domain scaling implied by Eq. (1). This is accomplished by scaling the integration limits with the domain size, so that $aq_l = bq_u = q_{\max}(t)$, where a and b are arbitrarily chosen to maximally exploit the available data. To do this we fixed a and b, determined an initial value for $q_{\max}$ by integrating over all of the data, computed a new q_l and q_u, recomputed $q_{\max}$ and continued to iterate. These partial scaled moments are strictly proportional to the true moments, but in practice we found that simply integrating over the finite data gave moments that scaled similarly to the partial scaled moments, i.e., $q_{\max}(t) \sim I_1(aq_{\max}, bq_{\max})/I_0(aq_{\max} bq_{\max})$.

The time dependence of the characteristic length is shown in Fig. 5 for peak-to-peak voltages of 0.56, 1.25, and 2.5 kV across the 0.72-mm gap. At the earliest times the characteristic length is about $L(0)=1.9$ mm, after which a linear increase of $L(t)$ with $t^{2/5}$ is then observed at all voltages, with the growth rate increasing with voltage. In fact, a nonlinear least-squares fit to $L(t)=L(0)[1+(t/\tau)^{\alpha}]$ gives an average exponent of $\alpha=0.42$, but we plot against 2/5 since this is close. For spinodal decomposition in a system with a conserved order parameter it is thought that after a linear, Cahn-Hilliard-Cook regime there is a nonlinear growth regime with a characteristic length that increases like $q_{\max}^{-1} \sim t^{1/3}$. Thus, although the electrorheological phase transition has many of the salient features of two-dimensional spinodal decomposition with a conserved order parameter, the growth kinetics appears to be somewhat faster than $t^{1/3}$.

The dependence of the growth rate on voltage is shown in the inset graph in Fig. 5. The rate increases slightly less than linearly with voltage and so rules out the field-squared dependence one might naively expect by noting that the solvent friction is field independent and that a dipole attraction scales as the field squared. However, these observations can be understood within the framework of fluctuation-induced coupling between columns, discussed below.

Finally, we completed studies of the dependence of column formation on the colloid volume fraction ϕ_c. The results in Fig. 6 show that the initial length scale *decreases* with increasing concentration, but that the growth rate *increases* with concentration, causing a crossover in the growth curves. These curves were best linearized with a growth exponent of 0.6, the disparity between this exponent and the 0.4 value in Fig. 5 being due to the intrinsic noise in the experiment. To first order the initial length scale should

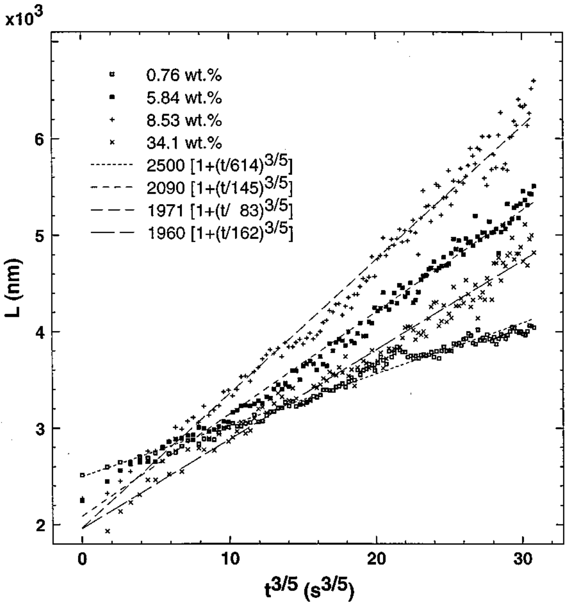

FIG. 6. The coarsening kinetics was also determined as a function of the initial particle volume fraction (the legend gives the colloid concentration in wt. %). As expected, the initial column spacing $L(0)$ decreases with increasing concentration, whereas the column growth rate increases with increasing concentration, causing a crossover in the growth curves. The best power-law fit to these data is $L(t)=L(0)[1+(t/\tau)^{3/5}]$. This coarsening exponent of 3/5 is greater than the value of 2/5 obtained in our first experiments. This variation is due to the large intrinsic noise in the experiment; a realistic estimate of the growth exponent is 0.5 ± 0.1.

decrease as $1/\phi_c^{1/2}$, the mean separation between single chains that span the electrodes, and the data roughly bear this out. The faster growth rate occurs because closer chains ‘‘feel’’ a greater attraction.

C. Thermal theory of coarsening

The roughly linear dependence of the coarsening rate on electric field and the approximately root time dependence of the length scale of the condensed phase can be accounted for semiquantitatively if we suppose that coarsening is driven by thermally generated dipole moments. The electric field of perfectly ordered chains or columns of dipoles is short ranged, decaying exponentially as one moves away from the column in a transverse direction, with a range that is of the order of magnitude of the lattice spacing of the particles in the column. However, chains or columns of dipoles are essentially one-dimensional solids and are thus subject to strong Landau-Peierls fluctuations. If the phonon field (longitudinal or transverse) of a column is $u(k)$, with k the wave vector along the column, then equipartition implies that [22]

$$|u(k)|^2 \sim \frac{k_B T}{\beta^2 E^2 R^3}, \tag{3}$$

where R is the radius of the column and $\beta^2 E^2 R^3$ is the energy scale for density fluctuations of the column.

These density fluctuations lead to the appearance of a fluctuating electric field near the column. It is easy to show that this electric field is of the order of magnitude [12]

$$\langle E^2 \rangle \sim \frac{k_B T R}{\rho^4} \tag{4}$$

at a transverse distance ρ from the column. Thus there is a fluctuating force E_{dip} per unit length between columns of radius R separated by a distance ρ, which may be either attractive or repulsive and is of the order of magnitude

$$F_{\mathrm{dip}} \sim \frac{\sqrt{k_B T}\beta E R^{3/5}}{\rho^3} \tag{5}$$

since the dipole moment per unit length of a column is $\beta E R^2$.

The dominant force for columns separated by a distance ρ comes from fluctuations with $k \sim \rho^{-1}$, thus the coherence length of these fluctuations will be $\sim \rho$. Now adjacent sections of length ρ, which will be pulled in different directions by this force, cannot move independently of one another because there is a strong restoring force, on the energy scale of $\beta^2 E^2 R^3$, which keeps the columns parallel to the field. We do expect, however, that sections of length $\xi \gg \rho$ can move independently, where ξ is determined by balancing this restoring force with the statistical average of the thermal force for a column of length ξ. We thus conclude that ξ satisfies

$$\sqrt{\xi\rho} F_{\mathrm{dip}} \sim \beta^2 E^2 R^3 \left(\frac{\rho}{\xi^2} \right), \tag{6}$$

which leads immediately to $\xi \sim \rho(\lambda/\phi)^{1/5}$.

The time scale for the columns to be drawn together by this force can be obtained by balancing this thermal force (for a column of length ξ) against the viscous force $F_{\mathrm{vis}} \sim C\mu_0 v \xi$, where μ_0 is the solvent viscosity, v is the velocity of the column, and C is a drag coefficient at most logarithmically dependent on R [23]. We thereby obtain a collision time

$$\tau_c \sim \frac{\mu_0 \rho^{3/2} C \lambda^{1/10}}{\sqrt{k_B T}\beta E \phi^{27/20}}. \tag{7}$$

We should compare this time to the coherence time of the fluctuations of the dipole moment on a scale $k=\rho^{-1}$. By the fluctuation-dissipation theorem we expect that the time for these fluctuations to dissipate is $\tau_f \sim 1/Dk^2$, where $D \sim k_B T/\mu_0 R$ is a characteristic diffusion coefficient for the particles [24]. We thus conclude that for large λ we will have $\tau_f \gg \tau_c$ and the fluctuations will persist long enough to drive coarsening. We now obtain the estimate

$$\rho(t) \sim (At)^{5/9}, \tag{8}$$

with $A \sim (\beta E)^{4/5}$, in qualitative agreement with the results above.

We conclude that the evolution of structure in an ER fluid proceeds by an unstable concentration fluctuation whose characteristic size scale increases with a power of time. The observed growth exponent of 0.5 ± 0.1 is slightly larger than the 1/3 value expected for spinodal decomposition and somewhat smaller than the 5/9 value predicted by extending the Halsey-Toor theory to account for electric-field-dependent fluctuations in interchain interactions. However, the fact that

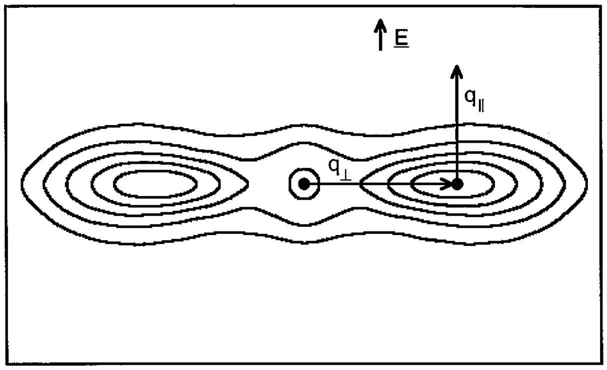

FIG. 7. This diagram shows the definition of scattering wave vectors $q_\parallel$ and $q_\perp$ used to describe the detailed shape of the two-dimensional scattering function. The contour lines are from real scattering data.

the characteristic growth rate increases almost linearly with the field is further evidence that the modified Halsey-Toor theory accounts for the structural evolution in this system.

D. Structure parallel to the field

We have thus far limited our discussion to the scattered intensity as a function of the wave vector $q_\perp$ in the direction parallel to the scattering lobes, which is perpendicular to the electric field. Nelson and Seung [25] have studied the statistical mechanics of line liquids and have noted a striking resemblance of the shape of our scattering images to predictions for line liquids. In this section we explore these connections quantitatively. Before we start our discussion it is useful to examine Fig. 7 to see how a wave vector $q_\parallel$ that is parallel to the applied field for each value of $q_\perp$ is defined.

There are several experimental issues to address. Is the shape of the scattering lobes scale invariant? How does the width of a scattering lobe vary along its length? What is the functional form of the scattered intensity in the parallel direction, that is, $I(q_\parallel, q_\perp = c)$? We will examine each of these issues experimentally and then will compare our results to theory.

The first issue we will investigate is the variation of the scattering width parallel to the field as a function of the scattering wave vector $q_\perp$. To do this it is useful to define the parallel moment

$$\langle q_\parallel^{1/2} \rangle = \int_0^\infty q_\parallel^{1/2} I(q_\parallel, q_\perp) dq_\parallel \Big/ \int_0^\infty I(q_\parallel, q_\perp) dq_\parallel .$$

We have chosen to work with root moment to eliminate convergence problems with the integrals, as the intensity falloff is expected to be Lorentzian in the direction parallel to the field. The results are shown in Fig. 8 for a sample subjected to a 0.56-kV/mm field at various aging times. A deep minimum in the width of the scattering function is observed at a value of $q_\perp$ that decreases with time and a master curve appears to be developing for values of $q_\perp$ past the minimum. The minimum scattering width occurs at the value of $q_\perp$ that maximizes the scattered intensity $I(q_\parallel = 0, q_\perp)$ and this value of $q_\perp$ is proportional to the moment $\langle q_\perp \rangle$ defined previously.

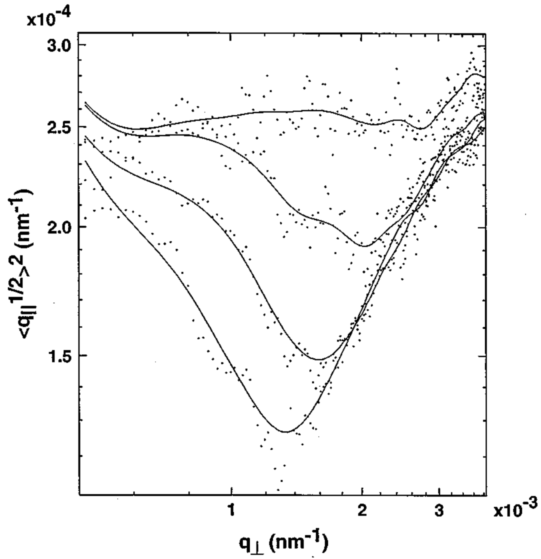

FIG. 8. The width of the scattering lobe in the $q_\parallel$ direction is a minimum at the value of $q_\perp$ where the intensity is a maximum. The scattering width is apparently time independent for values of $q_\perp > q_{\perp,\max}$. The solid lines are the data smoothed by Fourier filtering.

We can determine whether the shape of the scattering function, hence the column structure, is scale invariant. A scale-invariant scattering function will have a minimum width $\langle q_\parallel^{1/2} \rangle^2$ proportional to the peak position. It is convenient to define the length $L_\parallel = 2\pi / \langle q_\parallel^{1/2} \rangle^2$ and determine if this is proportional to our previously defined length $L_\perp$. Data for a fluid subjected to a 0.56-kV/mm field are shown in Fig. 9. Despite the noise these data convincingly show that $L_\parallel \propto L_\perp$. Similar results are obtained at larger fields, so on

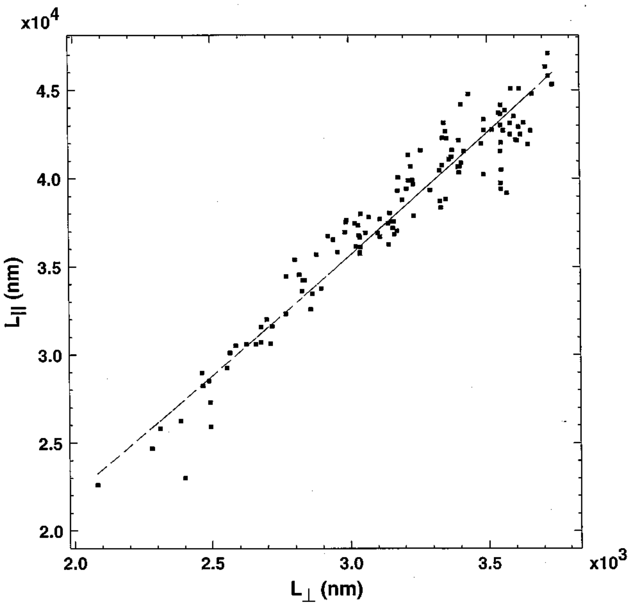

FIG. 9. The length $L_\perp$ is proportional to $L_\parallel$, indicating that the shape of the scattering data, and thus the domain structure, is scale independent. Note that there is roughly a one-decade difference in length scales, however, with correlations along the chains extending much further.

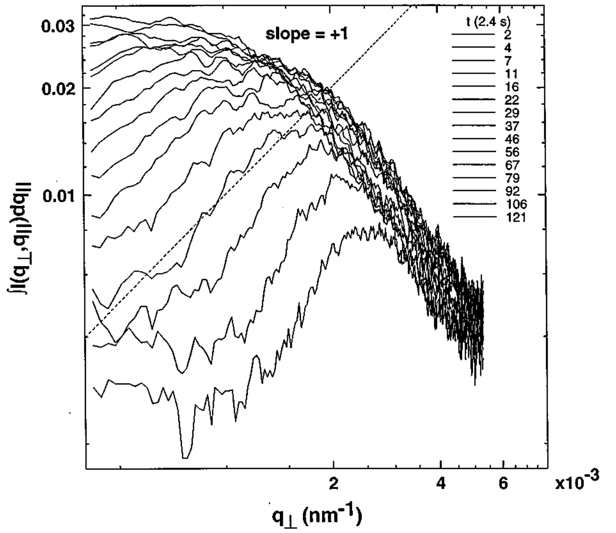

FIG. 10. The intensity integrated in the $q_\parallel$ direction should increase linearly with $q_\perp$, and this is found at all times. The same result is found at all voltages.

experimental grounds we conclude that the scattering function and column structure are scale invariant.

According to theory of line liquids, the integrated scattered intensity $\int_0^\infty I(q_\parallel,q_\perp)dq_\parallel$ should increase linearly with $q_\perp$ for $q_\perp < q_{\perp,\max}$. The data shown in Fig. 10 bear this out. This result is due to an underlying conservation law, as discussed below.

Finally, the theory of line liquids predicts that the line shape in the $q_\parallel$ direction is Lorentzian. Determining the line shape is difficult in such a noisy system, so we tried to take full advantage of our data in order to reduce the noise. To average the signal we (i) chose a value of $q_\perp$, (ii) computed the width $\langle q_\parallel^{1/2}\rangle^2$ and height $I(q_\parallel=0,q_\perp)$ of a 1-pixel-wide slice in the $q_\parallel$ direction at this $q_\perp$, and (iii) nonlinearly binned the normalized data $q_\parallel/\langle q_\parallel^{1/2}\rangle^2$ versus $I(q_\parallel,q_\perp)/I(q_\parallel=0,q_\perp)$ (the nonlinear bin widths were chosen to keep the signal-to-noise ratio fixed). This was repeated for each value of $q_\perp$ to obtain a signal-averaged data set at one particular coarsening time. In Fig. 11 we show the resultant time dependence of the line shapes. At early times the data are well described by a Lorentzian, but at later times they decrease more rapidly than Lorentzian for large $q_\parallel/\langle q_\parallel^{1/2}\rangle^2$. This may indicate that the line liquid theory only holds shortly after chain formation. Taken as a whole, the agreement between the experimental data and the line liquid theory is compelling at short times.

E. Line liquid theory

The intensity plots of the structure function of the ER fluid at short times after the field is applied is reminiscent of the equilibrium structure factors of line liquids [25,26]. However, since the interactions between the chains of dipoles are attractive [12], it is clear that once the dipole chains are formed there is no equilibrium state until the dipole spheres condense into their final crystalline form [13–15].

Let us first review some generic features of an ensemble of directed lines. Most notably, if the lines go from the top to the bottom of the sample, there is an equation of continuity for the areal density $\rho(x,y,z)$, defined so that in an xy cross section at height z_0,

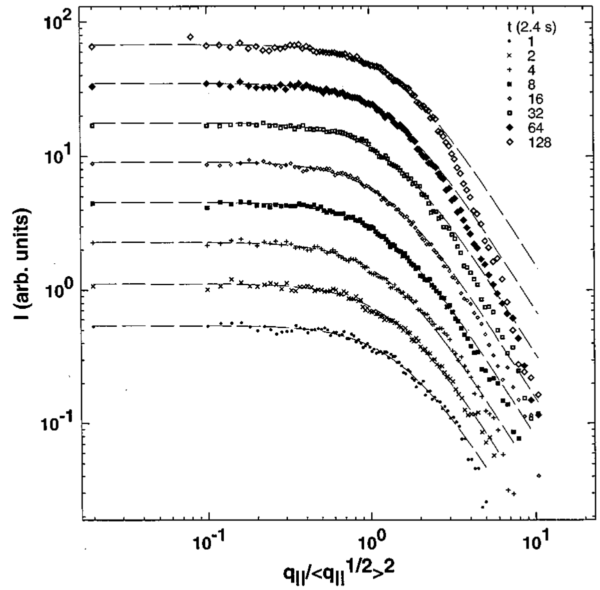

FIG. 11. The line shape of the scattering data in the $q_\parallel$ direction is fit to a Lorentzian (dashed lines) at various times after the field quench. At early times the fit is quite good, but at late times the scattered intensity decreases more rapidly than a Lorentzian.

$$\int \rho(x,y,z_0)dx\,dy = N(z_0), \tag{9}$$

where $N(z_0)$ is the number of dipole spheres in that section. If the chains are continuous from one electrode to the other, then it is clear that $N(z_0)$ will be independent of z_0. As with the continuity of charge this implies that

$$\frac{\partial\rho}{\partial z} + \vec{\nabla}_\perp\cdot\vec{t} = 0, \tag{10}$$

where $\vec{t}(x,y,z)$ is a vector in the xy plane and can be interpreted as the xy projection of the local tangent vector to the chains at (x,y,z) [26]. The conservation law implies that when $q_x = q_y = 0$, $\partial_z = 0$ or, in other words, $\delta\rho(0,0,q_z) = 0$, where $\rho(\vec{q}) = \rho_0 + \delta\rho(\vec{q})$. This implies that the structure function

$$S(\vec{q}) = \langle \delta\rho(\vec{q})\,\delta\rho(-\vec{q})\rangle \tag{11}$$

will vanish when $q_x = q_y = 0$. This is a generic feature of line liquids, independent of equilibrium, and is seen here in the data. Of course if the chains are broken or contain branches, the continuity equation will be modified by the addition of a source term. For large values of $\vec{q}$ the dipole chains will appear to be unbroken if the density of chain ends and branch points is low enough. At smaller $\vec{q}$ the structure function will cross over to that of an isotropic liquid, at long enough length scales even extended (but finite) objects will appear as points [26].

Equally generic to the structure function of line liquids is a peak at some value of $q_\perp$ corresponding to the average interchain spacing. This is simply due to the incipient liquid or crystalline order that will emerge at lower temperatures. Again, the data show these peaks.

To consider the dynamics of the coarsening, we note that the chains form almost immediately. Thus we can view the coarsening of the dipole fluid as the coarsening of a line gas suddenly quenched into the crystal phase and ignore the complication of chain formation. Note that although the number of dielectric spheres is constant with time, the number of chains need not be as they can join and coalesce even in the absence of chain ends and branch points. Thus we suggest a nonconserved coarsening dynamics. We model the change in areal density according to the Langevin equation

$$\frac{\partial \rho(x)}{\partial t} = -\Gamma \frac{\delta F[\rho]}{\delta \rho(x)} + \eta(x,t), \tag{12}$$

where $\eta(x,t)$ is a noise term with correlation chosen to ensure that the system comes to thermal equilibrium, namely,

$$\langle \eta(x,t)\,\eta(x',t')\rangle = \Gamma k_B T \delta^3(x-x')\,\delta(t-t'). \tag{13}$$

Using the model free energy [26] for a line liquid, we are led to the linearized equation for the structure function [27]:

$$\frac{\partial S(\vec{q};t)}{\partial t} \approx -2\Gamma\left[Cq_\perp^2 + K\,\frac{q_z^2}{q_\perp^2} + r\right] S(\vec{q};t) + 2\Gamma k_B T, \tag{14}$$

where $r<0$ and C and K are constants related to the stiffness and density of the dipole chains [26]. The nonlocal nature of the kernel in Eq. (14) is a consequence of the conservation law. For short times Eq. (14) can be solved and we find that

$$S(\vec{q};t) \approx e^{-w(\vec{q})t} S(\vec{q};0) + [1 - e^{-w(\vec{q})t}] S(\vec{q};\infty), \tag{15}$$

with $w(\vec{q}) = 2\Gamma[Cq_\perp^2 + K(q_z^2/q_\perp^2) + r]$. Thus the structure function will have the form of a line gas with an exponential $\vec{q}$-dependent decay. For $Cq_\perp^4 + Kq_z^2 > -rq_\perp^2$ the modes decay, while for $Cq_\perp^4 + Kq_z^2 < -rq_\perp^2$ the modes grow. Thus we expect that for very small q_z there will be a regime of $q_\perp$ for which the scattered intensity will grow at early times.

The structure function at zero time should be that of a line gas, namely,

$$S(\vec{q};0) \propto \frac{\rho_0^2 q_\perp^2}{Bq_\perp^2 + Cq_\perp^4 + Kq_z^2}, \tag{16}$$

where $B>0$ is related to the average spacing and this expression is valid for small $\vec{q}$. At larger $\vec{q}$ there will be additional terms leading to the peak that represents the average chain spacing. This form also predicts that at fixed $q_\perp$ the structure function will fall off along q_z with a Lorentzian line shape, in agreement with the data.

The three-dimensional structure function gives us information about the two-dimensional structure as well. Since the two-dimensional structure function $S_2(x,y) = S(x,y,z=0)$ we have

$$\begin{aligned} S_2(\vec{q}) &= \int e^{i(q_x x + q_y y)} S(x,y,z=0)\,dx\,dy \\ &= \int e^{i(q_x x + q_y y)} S(x,y,z)\,\delta(z)\,dx\,dy\,dz \\ &= \int S(q_x,q_y,q_z)\,\frac{dq_z}{2\pi}, \end{aligned} \tag{17}$$

where the last equality comes from the convolution theorem. The data have been reduced to this form by integration along q_z. We see again two generic features of the line liquid. The plot of $I(q_\perp) = q_\perp^2/S_2(q_\perp)$ versus $q_\perp$ should rise linearly at small $q_\perp$ and then have a dip at $q_\perp^*$, the wave vector of the incipient crystalline order at the relevant density. According to the model outlined above, $I(q_\perp) \propto \sqrt{Bq_\perp^2 + Cq_\perp^4}$, in agreement with the data for small $q_\perp$. We may also look at the time dependence of $I(q_\perp;t)$. Using Eqs. (15) and (17) we have

$$I(q_\perp;t) \propto e^{2\Gamma(r-B)t} I(q_\perp;0) \tag{18}$$

for small times.

While there is no time at which an equilibrium line liquid exists, at short enough times the system is not far from the dilute gas that it started as on its way to a crystal. A more detailed theory of the coarsening would require the introduction of nonlinearities along the lines of Langer, Bar-on, and Miller [28].

IV. STEADY SHEAR

The shear thinning of the fluid viscosity μ is perhaps the most basic aspect of electrorheology. For the colloidal silica fluid studied here we found [16] that at low applied fields the viscosity shear thinned as $\mu \sim \dot{\gamma}^{-2/3}$, where $\dot{\gamma}$ is the shear rate, whereas at high applied fields the standard result $\mu \sim \dot{\gamma}^{-1}$ was obtained. The discovery of the anomalous 2/3 shear thinning exponent prompted the development of the independent droplet model, which gives this exponent. This model makes some very specific predictions about the droplet size and orientation as functions of the shear rate and field and these can be determined by light scattering. Likewise, the kinetic chain model, originally developed to account for oscillatory shear, gives a shear thinning exponent of -1 and makes dramatically different predictions for the chain orientation. In the following we report measurements of the orientation of particle structures and compare these to the kinetic and equilibrium models.

A. Droplet fragmentation and orientation

When an ER fluid is subjected to shear, the columns fragment and tilt in response to the hydrodrodynamic forces, resulting in several changes in the light-scattering pattern (Fig. 12). First, the coarsening of the lobes stops and the scattering pattern reaches a steady state, as shown in Fig. 13. Second, the scattering pattern is rotated in the direction of fluid vorticity. Finally, the peak of the scattering lobes decreases to $q=0$ (Fig. 14), showing that the quasiperiodic intercolumn correlations are destroyed. These observations indicate rotated structures whose spatial correlations have

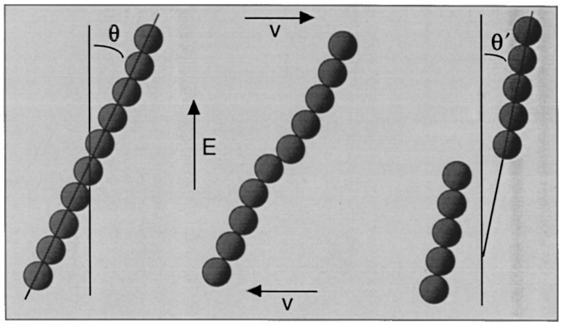

FIG. 12. When an ER fluid is subjected to steady shear the columns fragment into droplets that tilt in the direction of the fluid vorticity to some equilibrium angle θ_{max} relative to the electric field. A more subtle change is that the maximum of the scattering lobes moves to zero scattering wave vector, indicating a loss in spatial correlation between droplets.

been destroyed by shear. By measuring the degree of rotation as a function of shear rate, we can directly test models of the steady-state fluid structure.

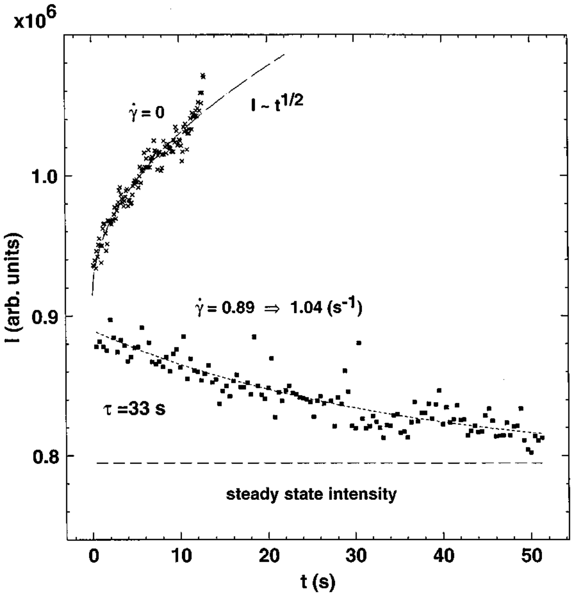

FIG. 13. In steady shear the scattering pattern reaches a steady state, in contrast to the coarsening that occurs in the quiescent fluid. These data show how the scattered intensity approaches a steady state after the shear rate is increased from 0.89 to 1.04 s^{-1}. The decay time of 33 s is quite large compared to the reciprocal shear rate, indicating that the droplet-droplet collision time may be an important time scale.

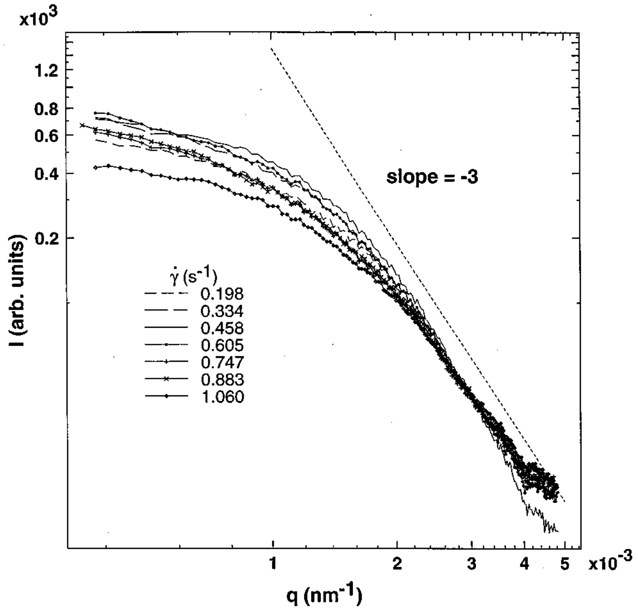

FIG. 14. A radial slice of the scattered intensity taken through the center of the tilted lobes shows that the maximum scattered intensity occurs at zero-scattering wave vector, unlike in the quiescent fluid, where a peak occurs at finite q.

To characterize the scattering data it is necessary to have a systematic method of determining the angle θ_{max} by which the scattering lobes of the sheared fluid are rotated relative to those of the quiescent fluid. In the following, positive θ_{max} indicates a rotation in the direction of the fluid vorticity. To determine θ_{max} we first divide a time-averaged scattering image into 360 wedges that each subtend 1° of arc. The scattered intensity in each wedge is computed by integrating the intensity from the experimentally determined limits q_l to q_u. We have termed this technique ''longitudinal'' scattering analysis [7] by analogy to the latitudes and longitudes of the Earth; if the laser beam is considered as the axis, then we have integrated over the latitudes to obtain the intensity as a function of longitude. Furthermore, the prime meridian is orthogonal to the direction of the electric field.

In Fig. 15 we contrast the longitudinal analysis for the quiescent fluid with that of a fluid sheared at a rate of 1.06 s^{-1}. The scattering maximum of the sheared sample is shifted to positive θ and the scattering half-width σ is broader than in the sheared fluid. The peak position and half-width were extracted by fitting the Gaussian $I(\theta)=I(0)e^{-(\theta-\theta_{\mathrm{max}})^2/2\sigma^2}$ to the data (Fig. 16), which worked well, despite the slight bilateral asymmetry of the scattering lobes.

We first investigated the dependence of the droplet orientation on the applied electric-field frequency. This dependence is shown in Fig. 17 for a sample at 0.8 kV and a shear rate of 1.4 s^{-1}. Because the angular displacement is nearly constant over this frequency regime, we can conclude that the polarizability is essentially frequency independent. We arbitrarily chose 1.0 kHz as the standard operating frequency for our studies, although some shear rate studies were also done at 400 Hz. It is worth noting that because the particle polarizability is fast and the shear rate is slow, there is no chance of dephasing the particle dipoles by particle rotation. Particle dephasing would reduce the dipolar interactions at high shear rate.

The dependence of the droplet rotation angle with shear rate is shown in Fig. 18. These data were taken at an applied frequency of 400 Hz and at a peak-to-peak voltage of 1.2 kV across the 1.0-mm gap. A nonlinear least-squares power-law fit to the data gives $\theta_{\mathrm{max}} \sim \dot{\gamma}^{0.326}$, so good linearity is obtained by simply plotting θ_{max} against $\dot{\gamma}^{1/3}$.

This cube-root dependence is much weaker than one might naively expect. For a rigid rod in shear the electrostatic torque that tends to maintain field alignment increases

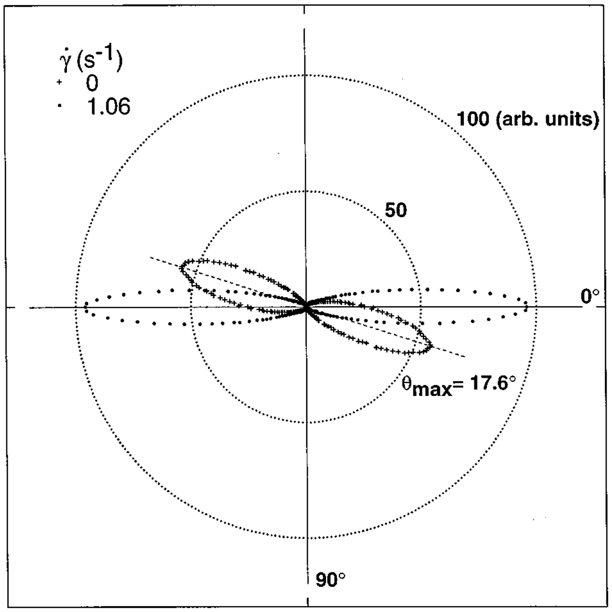

FIG. 15. The radially integrated intensity of scattered light, obtained from the longitudinal analysis, is shown for an unsheared and sheared sample in the polar coordinates (I,θ). Positive angles are in the direction of fluid vorticity and the small background scattering has been subtracted for clarity. Note that for the sheared sample the scattering pattern is angularly displaced, indicating column tilting; broadened, indicating a dispersity of column sizes; and skewed, primarily because of the nonlinear dependence of the orientation angle on droplet size.

to first order as the tilt angle θ, whereas the hydrodynamic torque increases as the shear rate $\dot{\gamma}$. In steady state the droplet velocity is zero, so a torque balance gives the linear relation $\theta_{\max}\sim\dot{\gamma}^1$. The sublinear dependence actually observed is due to the tendency of chains or droplets to fragment in response to flow, as discussed below.

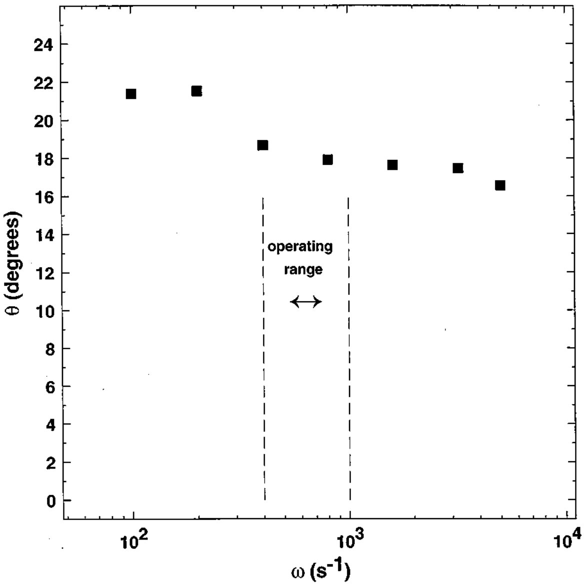

FIG. 17. The dependence of the droplet orientation angle on the field frequency is shown for a 7.5-wt. % sample at 0.8 kV applied across the 1.0-mm gap and a shear rate of 1.4 s^{-1}. The angular displacement is nearly constant in this regime, indicating that the particle polarization is nearly frequency independent. Most of our shear and voltage studies were done at 1.0 kHz, although some shear rate studies were done at 400 Hz. Because the particle polarizability is fast and the shear rate is slow, the particle dipoles will not dephase by rotation in shear.

The droplet or chain orientation angle can also be studied as a function of the applied electric field at constant shear rate. Stronger fields should align the structures more closely

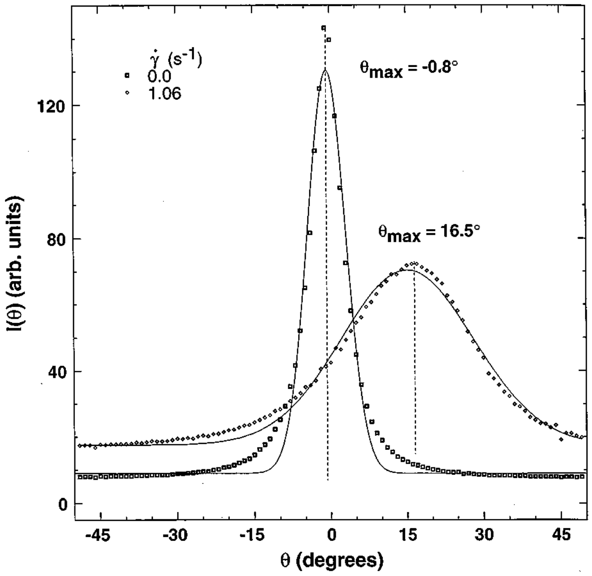

FIG. 16. The column orientation can be obtained from a Gaussian fit (lines) to the data or from the position of the intensity maximum. The Gaussian does not fit the wings of the data very well, but reliably finds the peak position, while being insensitive to noise. The intensity is radially integrated.

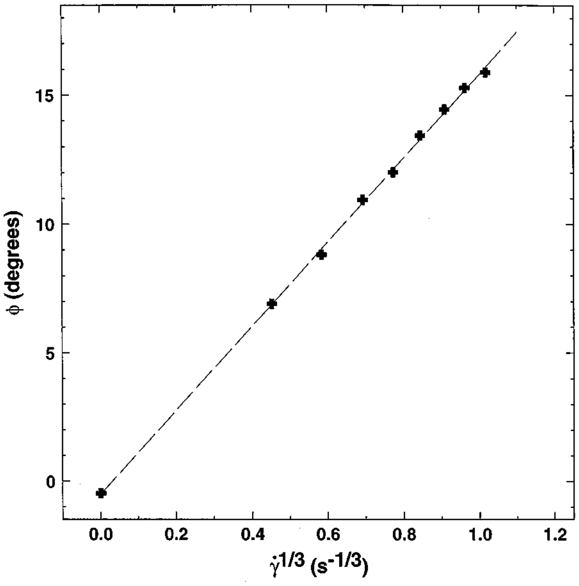

FIG. 18. The linear increase of the droplet orientation angle with the cube root of the shear rate bolsters the independent droplet model of the shear thinning viscosity. This sample was 7.5-wt. % silica and the applied voltage was 1.2 kV at 400 Hz across the 1.0-mm gap.

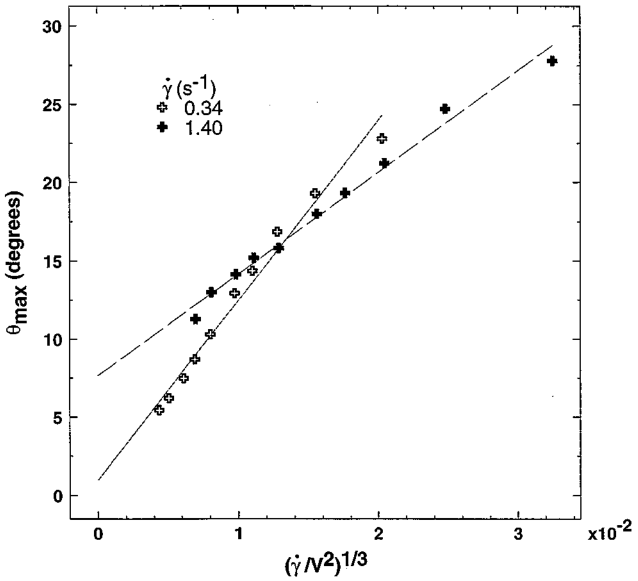

FIG. 19. The orientation angle is shown as a function of the applied field, at constant shear rate, for a 7.5-wt. % silica fluid. Because the fluid is nonohmic at high voltages, it is expected that the particle and fluid polarizabilities will be field dependent, thus obscuring the scaling. Still, at the lower shear rate of 0.34 s^{-1} the data are in good agreement with the expected cube root law. At the higher shear rate the data are better described by a smaller exponent, near 0.2, perhaps due to the formation of a shear slip instability.

with the field. Because the fluid is non-Ohmic at high voltages, it is expected that the particle and fluid polarizabilities may be field dependent, so the scaling is expected to be somewhat obscured. Still, Fig. 19 shows that the data at a shear rate of 0.34 s^{-1} are in good agreement with the cube-root law obtained in the shear-rate-dependent studies. We will now compare these observations with the predictions of the models.

B. Independent droplet model

Here we give a brief derivation of the independent droplet model first developed to describe the shear thinning viscosity of an ER fluid. This model neglects droplet-droplet hydrodynamic and electrostatic interactions and so is most appropriate for dilute suspensions at low Mason numbers, yet it remains informative for larger values of the concentration.

This independent droplet model is based partly on the result of Halsey and Toor [13] for the shape of a particle droplet. By balancing depolarization effects against surface tension, one finds that such an independent droplet is roughly a prolate sphere, with the size c of the droplet in the direction parallel to the applied field related to the size b of the droplet in the direction perpendicular to the field by $b \sim r_d^{1/3} c^{2/3}$, where r_d is the radius of an colloidal particle.

In shear flow an ellipsoidal droplet will rotate so that its long axis is no longer parallel to the field. The larger the droplet, the greater the rotation in a shear flow. This rotation reduces the depolarization energy of a droplet and a balance between depolarization energy and surface energy determines the characteristic droplet size. This size computation leads to a shear-rate-dependent ER fluid viscosity.

In the following the electric field is oriented along the z direction and the shear flow is $v(z) = \dot{\gamma} z \hat{x}$. We also assume a solvent dielectric constant $\varepsilon_s = 1$. The hydrodynamic torque about the y axis for a rigid ellipsoidal droplet rotating at a rate $\dot{\theta}$ in a shear flow $\dot{\gamma}$ is given by [29]

$$L = \frac{2\mu_0 V}{b^2 n_x + c^2 n_z} [(c^2 \cos^2\theta + b^2 \sin^2\theta)\dot{\gamma} - (b^2 + c^2)\dot{\theta}], \tag{19}$$

where V is the spheroid volume and $n_{x,y,z}$ are the shape-dependent depolarization factors of the spheroid. The depolarization factors of a prolate spheroidal droplet can be expressed as $n_z \equiv n$ and $n_{x,y} \equiv (1-n)/2$. For extremely prolate spheroids with $c \gg b$, we can define $g \equiv b^2/c^2 \ll 1$ to obtain [29] $n \approx -\frac{1}{4} g$, where we have dropped a logarithmic term. Thus both g and n are suitable small parameters for expansion.

If the droplet is in mechanical equilibrium, then the hydrodynamic torque L must balance the electrical torque K. The electrostatic torque K on a spheroid of dielectric constant ε inclined at an angle θ to the field is [30]

$$K \cong -\frac{(\varepsilon-1)^2}{8\pi(\varepsilon+1)} E^2 V \sin(2\theta), \tag{20}$$

where E is the applied electric field.

If we assume that the droplet angle θ is small, then balancing the electrostatic and hydrodynamic torques gives

$$\theta \approx \frac{16\pi(\varepsilon+1)\mu_0 \dot{\gamma}}{(\varepsilon-1)^2 E^2} \frac{1}{g} \propto \frac{\mathrm{Mn}}{g}. \tag{21}$$

$\mathrm{Mn} = \mu_0 \dot{\gamma} / 2\varepsilon_0 \varepsilon_c \beta^2 E_0^2$ is the Mason number, which expresses the ratio of hydrodynamic to electrostatic forces between two vicinal spheres in shear in terms of the dielectric contrast factor $\beta = (\varepsilon_p - \varepsilon_c)/(\varepsilon_p + 2\varepsilon_c)$, where ε_p is the particle dielectric constant, ε_c is the dielectric constant of the continuous phase, and $\varepsilon_0 = 8.854 \times 10^{-14}$ F/cm is the vacuum permittivity. Note that for a rigid droplet with a large aspect ratio in a large shear gradient, the tilt angle will be large, causing the droplet to gain polarization energy. It is therefore reasonable to expect the droplet to attempt to minimize its total energy by reducing its size, even at the expense of increasing its surface energy per unit volume.

Having determined the tilt angle θ as a function of $g = b^2/c^2$, we can now find the size and aspect ratio of a droplet that minimize its total energy. This is done by balancing the depolarization energy (which will be a function of n and θ, both small parameters) against the surface tension of a droplet.

The depolarization energy of a spheroid is [30]

$$F_d \approx -\frac{(\varepsilon-1)VE^2}{8\pi} \left[1 - \left(\frac{\varepsilon-1}{\varepsilon+1} \right) \theta^2 - (\varepsilon-1)n \right], \tag{22}$$

where only the lowest-order terms in θ and n have been kept. This energy is minimized when $\theta = 0$ and $n = 0$, so this term favors long, thin columns aligned with the field. On the other hand, the surface energy term

$$F_s = \frac{\tilde{s}(\varepsilon-1)E^2 S}{4\pi} \tag{23}$$

favors large spheroidal droplets. Here $S = 4\pi(abc)^{2/3}$ is the surface area of the spheroid and we expect $\tilde{s} \sim r_d$ [13,31].

Minimizing the total energy $F_d + F_s$ gives $g \propto \mathrm{Mn}^{2/3}$, $b \propto \mathrm{Mn}^{-2/3}$, and $c \propto \mathrm{Mn}^{-1}$. The droplet width is $b \propto c^{2/3}$, as in the theory of the quiescent fluid [6]. Also, since $\mathrm{Mn}/g \propto \mathrm{Mn}^{1/3}$, Eq. (4) indicates that $\theta \propto \mathrm{Mn}^{1/3}$ for $M \ll 1$, which confirms that θ is small. Thus, as the shear rate increases (or the electric field decreases) the droplet length c and its aspect ratio $c/b \propto \mathrm{Mn}^{-1/3}$ decrease while the tilt angle increases.

The dependence of the droplet orientation angle has a direct bearing on the fluid viscosity. The field enhancement of the viscosity is conveniently quantified by the dimensionless *field-specific* viscosity $\mu_F \equiv (\mu - \mu_\phi)/\phi\mu_0$, where μ_ϕ is the solution viscosity at infinite Mn. To determine the droplet contribution to the shear part of the stress tensor we compute the hydrodynamic torque per unit volume in the fluid. If the volume fraction of droplets is ϕ, then this is $\tau_h \cong \phi 4\mu_0 \dot{\gamma}/g$, which yields

$$\mu_F \propto \mathrm{Mn}^{-2/3} \tag{24}$$

for the field-induced contribution to the shear-thinning viscosity. This calculation applies only to the intermediate Mason number regime where the Mason number is small enough for chains to form, yet not so small that these chains span the electrode gap.

C. Chain model

We have recently developed a simple chain model [17] of electrorheology that is based on a balance of electrostatic and hydrodynamic forces. This *athermal* model was originally based on the interaction between the induced dipole moments of dielectric spheres in solution. The dipole moment was originally computed for a single sphere in a liquid continuum, but we have modified this model to account for local-field effects by self-consistently computing the dipole moment on an enchained sphere. The presence of vicinal spheres then alters the local field and this has a substantial effect on the agreement of the model with experiment, as we shall see.

In the chain model the particle structures are presumed to be chains of spheres that interact through dipolar forces with their neighbors. The self-consistent electrostatically induced attractive dipolar force is [17]

$$F_{\mathrm{sc}} = b\zeta(3)[(3\kappa_1\cos^2\theta - \kappa_2)\hat{\mathbf{r}} + \kappa_3\sin(2\theta)\hat{\boldsymbol{\theta}}], \tag{25}$$

where $b = 3\pi a^2\mu_0\dot{\gamma}/8\ \mathrm{Mn}$, $\zeta(3) \cong 1.202$ is the Riemann zeta function, and $\hat{\mathbf{r}}$ and $\hat{\boldsymbol{\theta}}$ are unit vectors parallel and perpendicular to the line of centers between the spheres. The remaining constants have to do with the local-field effects and are given by

$$\kappa_1 = \frac{1+\chi^2/8}{(1-\chi/4-\chi^2/8)^2},$$

$$\kappa_2 = \frac{1}{(1+\chi/4)^2}, \tag{26}$$

$$\kappa_3 = \frac{1}{1-\chi/4-\chi^2/8},$$

where $\chi = \beta\zeta(3)$. To obtain some idea of the magnitude of the local-field correction, the enhancement, over the dipole approximation, of the breaking strength of a chain in tension aligned along the field direction is $\zeta(3)(3\kappa_1 - \kappa_2)/2$. For $\beta = -\frac{1}{2}$ this factor is 0.71, but for $\beta = 1$ the enhancement is 7.54.

The fluid exerts a Stokes friction on each of the spheres and thus a hydrodynamic torque on the chain. Balancing this hydrodynamic torque against the electrostatic torque, obtained by summing the tangential component of the dipolar force along the chain, gives $\kappa_3\zeta(3)\tan\theta = 8\ \mathrm{Mn}N^2$ for the tilt angle of a chain of $2N+1$ spheres. Balancing the hydrodynamically induced tension at the chain center against the radial component of the dipolar force gives the mechanical stability constraint

$$\zeta(3)\ \frac{3\kappa_1\cos^2\theta - \kappa_2}{\sin\theta\ \cos\theta} \geqslant 16\ \mathrm{Mn}N^2. \tag{27}$$

The chain angle thus increases with chain length. The longest stable chain will have a critical chain angle that depends on the dielectric contrast through

$$\tan\theta_c = \sqrt{\frac{3\kappa_1 - \kappa_2}{2\kappa_3 + \kappa_2}} = \sqrt{\frac{2}{3}}\,\frac{1+\chi/4}{\sqrt{1-\chi/2}}. \tag{28}$$

(Note that the singularity is outside the physical range of β.) The chain angle is also closely approximated by the linear relation $\sin\theta_c \cong \sqrt{2/5}(1+3\chi/10)$. As β increases over its maximum physical range of $-\frac{1}{2}$ to 1, the critical chain angle increases from 31.3° to 59.3°. A stable chain of maximum length $N \propto \mathrm{Mn}^{-1/2}$ will be oriented at exactly the critical angle θ_c. By contrast, the droplet model gives a ellipsoid length $L \propto \mathrm{Mn}^{-1/3}$ and an orientation angle increasing as $\theta \propto \mathrm{Mn}^{1/3}$.

The data clearly show a dependence of the chain angle on the cube root of Mn and so support the droplet model. However, electrode friction can affect the simple prediction of the chain model to give a linear increase of the critical angle with Mn.

Rheology

The viscosity can be computed in a straightforward fashion. The electrostatic torque on a single-particle pair is $2aF_{e,\theta} = 2a\zeta(3)\kappa_3 b\ \sin 2\theta$. There are $2N$ such pairs in a chain so the electrostatic torque per chain is $\tau_e = \frac{3}{2}\pi a^2\varepsilon_0\varepsilon_c\beta^2E_0^2L\zeta(3)\kappa_3\sin 2\theta$. In terms of the volume fraction ϕ of spheres the stress σ in the sample is thus $\sigma = \frac{9}{8}\varepsilon_0\varepsilon_c\beta^2E_0^2\phi\zeta(3)\kappa_3\sin 2\theta_c$. Using our result for the critical angle gives the shear field specific viscosity

$$\mu_F \cong c\ \mathrm{Mn}^{-1}, \tag{29}$$

where to a good approximation $c = \frac{1}{5}(\frac{3}{2})^{5/2}\zeta(3)(1 + \frac{4}{10}\beta + \frac{3}{20}\beta^2 + \frac{1}{6}\beta^3)$ over the physical range of β.

The scaling $\mu - \mu_\phi \propto \dot{\gamma}^{-1}$ has been obtained in many experiments, including those conducted on our silica fluid at

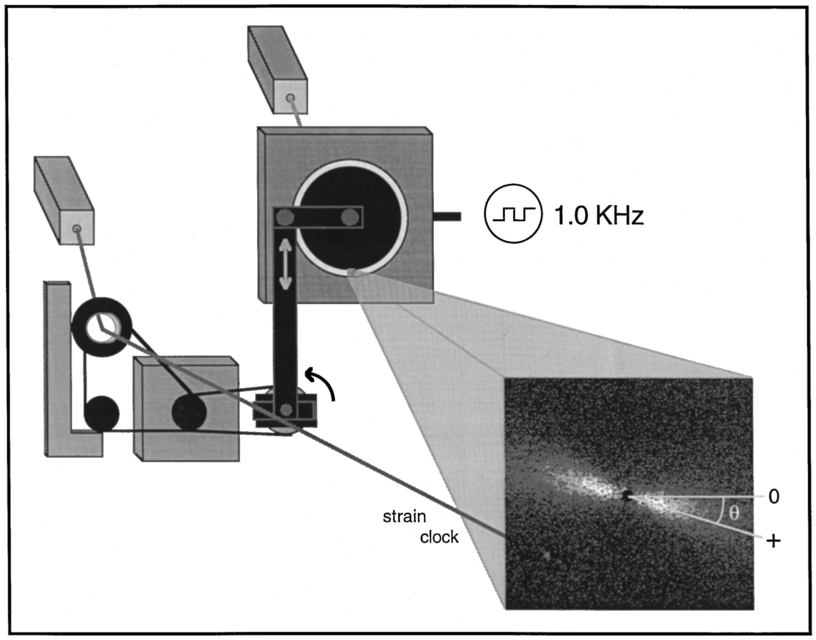

FIG. 20. A typical scattering image contains a pair of scattering lobes and the strain clock. These scattering lobes are tilted in the direction of fluid vorticity by some angle θ relative to the orientation of the scattering lobes obtained for the quiescent fluid, which are orthogonal to the electric-field vector.

high fields [16]. However, for the silica fluid at low fields we find $\mu-\mu_{\phi}\propto\dot{\gamma}^{-2/3}$, a result consistent with the elliptical droplet model [16].

V. OSCILLATORY SHEAR

We have reported preliminary measurements of ER fluids in oscillatory shear flow that demonstrate that the chain dynamics is highly nonlinear. The nonlinear dynamics was reasonably well described by a simple *kinetic* chain model, in which the nonlinear response is caused by large variations in the chain length during an oscillation. These chain length variations are caused by aggregation and fragmentation processes that occur during each cycle. At the time these results were reported we did not understand why the simple model we presented did not agree more quantitatively with experiment, nor did we have direct experimental evidence for the chain length variations assumed to drive the nonlinear response. In the time hence we have thoroughly examined the chain model, including such effects as local-field corrections, multipolar interactions, and hydrodynamic screening. Experimentally, we have now determined the chain size variations that occur during each cycle. We will first reexamine the kinetic chain model, showing how it can be modified to take into account these effects and then we will reanalyze previously reported data and present data on the fluctuations in chain size during a shear cycle.

We have previously generalized the droplet model to oscillatory shear at small strain amplitudes, where aggregation and fragmentation effects that occur during a cycle can be ignored. This model gives a sinusoidal response, but the single characteristic relaxation time of the system depends on the strain amplitude and shear frequency.

A. Data analysis

A scattering image contains a pair of scattering lobes and, of course, the strain phase clock, as in Fig. 20. These scattering lobes are tilted by an angle θ relative to the orientation of the scattering lobes obtained for the quiescent fluid. The angle θ was then obtained by one of two methods: locating the intensity maximum $\theta_{\max}$ or finding the median θ_m, defined as that angle that divides the integrated scattered intensity into equal halves, so $\int_{\theta_m}^{90°}I(\theta)d\theta=\int_{-90°}^{\theta_m}I(\theta)d\theta$. The latter method is used when the strongly nonlinear dynamics is characterized by twin peaks. Under these circumstances simply locating the maximum peak causes discontinuities in the data.

B. Measurements

At relatively low strain amplitudes the response of the orientation angle $\theta_{\max}$ to the sinusoidal shear strain $\gamma=\gamma_0\sin(2\pi\nu t)$ was nearly linear, demonstrating that fragmentation and aggregation effects may be not be important in perturbative flows where $\gamma_0\ll 1$. This quasilinearity is exemplified in Fig. 21, where Lissajous plots of $\tan(\theta_{\max})$ against γ are shown to be nearly elliptical. At the low shear frequency the chain orientation leads the strain by 57°. Since a 90° phase shift would put the droplets in phase with the strain rate, we conclude that the polarization coupling to the electric field, which tends to align the chains, dominates the hydrodynamic forces, so the chains deviate from field alignment only at the highest shear rates.

Conversely, at high frequencies the shear rate $\dot{\gamma}=2\pi\nu\gamma_0\sin(2\pi\nu t)$ is much larger and the droplet orientation is nearly in phase with the fluid shear since the hydrodynamic torque dominates the electrostatic torque. Note that under this condition the affine deformation limit is nearly achieved, as shown by the dashed line.

At higher strain amplitudes the motion becomes ‘‘clipped’’ as the droplets fragment and aggregate during the cycle in order to maintain good electric-field alignment. This nonlinear motion is evidenced by the parallelogram-shaped

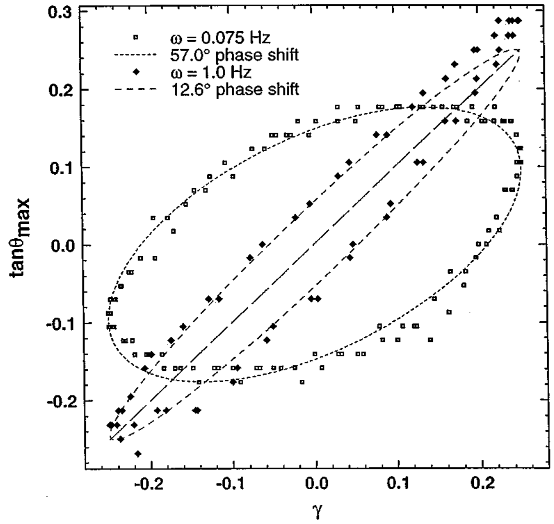

FIG. 21. Clockwise Lissajous plots of tan($\theta_{\max}$) against γ are virtually elliptical (lines) when the strain amplitude is small. At high strain frequency hydrodynamic forces dominate and the motion is nearly in phase with the strain. At low frequency the electrostatic forces dominate and the chains deviate from field alignment in proportion to the instantaneous strain rate, thus being almost out of phase with the strain.

Lissajous plots in Fig. 22. The dashed lines represent theoretical curves computed from the theory developed below.

At lower voltages we observe a different nonlinear fluid response, as shown in a Lissajous plot in Fig. 23, and against time in Fig. 24. The droplet motion leads the strain, indicating that electrostatic interactions dominate. This may seem surprising, given that the field is small, but we have also reduced the strain frequency to 0.075 Hz.

Another way to appreciate the nonlinear behavior of this system is the noncircular Lissajous plot of the chain angular velocity versus the chain angle (Fig. 25). Again, the theoretical prediction is shown for comparison.

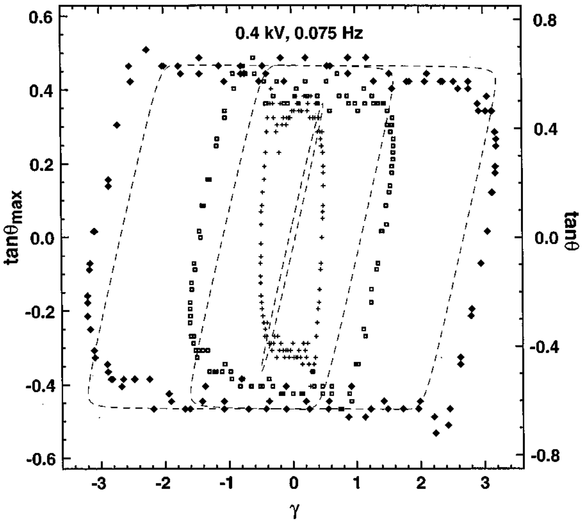

FIG. 22. Lissajous plots at strain amplitudes of $\gamma_0 = 0.5$, 1.6, and 3.2 have parallelogram shapes that indicate a ‘‘clipping’’ of the angular motion as chains fragment and align with the field at high strains. The theoretical curves (dashed lines) are computed in the instantaneous ‘‘equilibrium’’ limit where k is large.

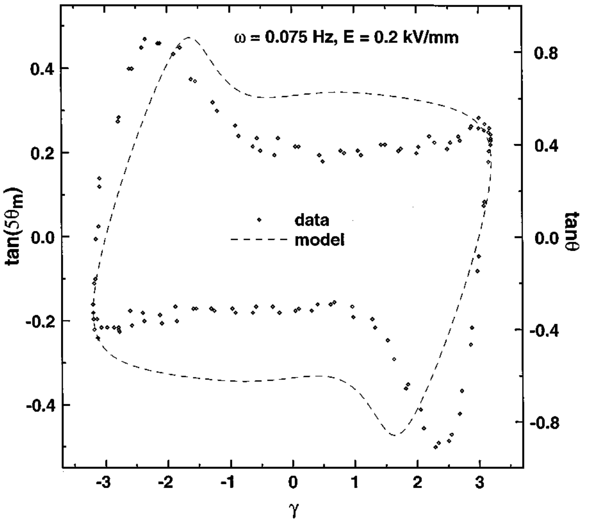

FIG. 23. At low voltages a different nonlinear response of the fluid can be observed, with retrograde motion of fragmenting chains. The dashed line is a theoretical curve. The amplitude of motion is sensitive to the dipolar model and the method of data reduction.

Starting at maximum positive strain, the droplet half cycle can be described as follows. As the strain reverses, the droplets corotate with the fluid and tilt to a maximum angle at roughly half the maximum strain on the return stroke, whereupon they fragment and undergo retrograde motion to realign with the electric field. If inertial effects are neglected then the hydrodynamic torque equals the electrostatic torque, so at zero tilt angle the droplets corotate with the fluid. Because the hydrodynamic torque is thus proportional to the droplet tilt angle, the large area within the Lissajous loop indicates that this nonlinear response is dissipative.

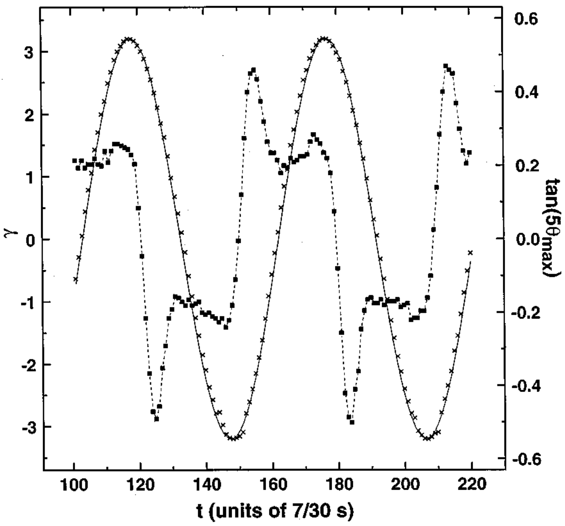

FIG. 24. The ‘‘dogbone’’ nonlinearity shown in Fig. 23 is plotted against time. The strain data are fit to a sinusoid (solid line) and the chain orientation data are connected by a dashed line. The retrograde motion is quite evident in this representation.

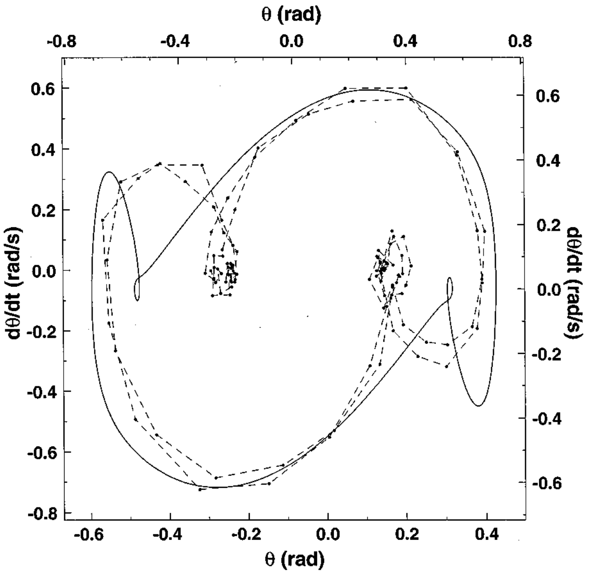

FIG. 25. The nonlinear response is shown as a Lissajous plot of chain angle versus angular velocity. The solid line is the theoretical prediction of the chain model and is plotted against the top and right axes; the data are plotted against the bottom and left axes.

Finally, we observed that the scattering lobes brighten considerably as they swing back through zero angle, indicating droplet aggregation. Likewise, as the lobes swing to their maximum tilt they diminish in intensity, indicating droplet fragmentation. All of these observations of the droplet motion point the way to the simple model of the dynamics that we shall now present.

C. Kinetic chain model

The salient features of experimental results we have shown can be understood in terms of a kinetic model of the dynamics of volatile chains. We have presented this model elsewhere [17] for the case of fixed induced dipolar interactions: Here we modify the basic model to account for local-field corrections. Local-field corrections have the important consequence of changing the critical chain angle from a fixed value of ~39.2° to a range from 31.3° to 59.3°, depending on the dielectric contrast factor β.

We consider a linear chain of $2N+1$ spheres of radius a labeled from $-N$ to N in a coordinate system (x,z), the origin of which is centered on the zeroth sphere (Fig. 26). The z axis is in the direction of the electric field and the x axis is in the direction of fluid vorticity. The chain makes an angle θ to the x axis, so the position of the kth bead is $(2ak\ \sin\theta, 2ak\ \cos\theta)$. The fluid velocity is given by $v(z)=\dot{\gamma}z\hat{x}$, where $\hat{x}$ is a unit vector, and the velocity of the kth bead is $v_k=2ak\dot{\theta}(\cos\theta\hat{x}-\sin\theta\hat{z})$ for a chain rotating at angular velocity $\dot{\theta}$.

The shearing fluid exerts a hydrodynamic force $\mathbf{F}_k=6\pi\mu_0[v(z)-v_k]$ on the kth bead, where μ_0 is the liquid viscosity. This hydrodynamic force can be decomposed into a tangential component that causes chain rotation and a component that causes tension or compression. The tangential component of the hydrodynamically induced force between the kth and $(k+1)$th spheres is

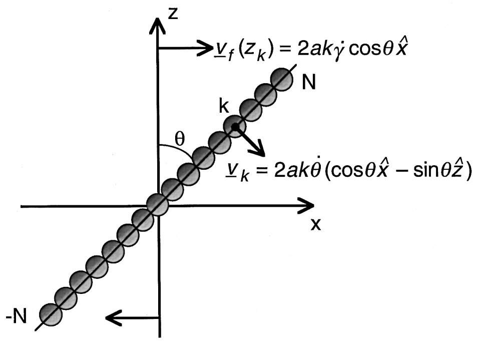

FIG. 26. The coordinate system used in the kinetic chain model. The number of spheres in the chain is $2N+1$, v_k is the velocity of the $+k$th bead, and v_f is the fluid velocity.

$$F_{h,\theta}=\sum_{k+1}^{N} F_k\cdot(\cos\theta,-\sin\theta)$$

$$\cong 6\pi\mu_0 a^2(\dot{\gamma}\cos^2\theta-\dot{\theta})(N^2-k^2).$$

This tangential force is a maximum at the chain center, where in low-Reynolds-number flow it is balanced solely by the tangential component [Eq. (25)] of the dipole-dipole interaction force

$$F_{\mathrm{sc},\theta}=\zeta(3)(3\pi a^2\mu_0\dot{\gamma}/8\ \mathrm{Mn})\kappa_3\sin 2\theta.$$

Balancing the tangential hydrodynamic and electrostatic forces at the chain center gives the damped oscillator equation

$$\dot{\theta}+\omega_d\sin 2\theta=\dot{\gamma}\cos^2\theta \quad \text{where} \quad \omega_d=\frac{\zeta(3)\kappa_3\dot{\gamma}}{16\ \mathrm{Mn}N^2}. \tag{30}$$

The characteristic oscillator frequency ω_d depends strongly on chain size. Physically acceptable values N must correspond to mechanically stable chains or fragmentation will occur. The radial component (directed along the chain axis) of the hydrodynamic force is

$$F_{h,r}=\sum_{k+1}^{N} F_k\cdot(\sin\theta,\cos\theta)=3\pi\mu_0 a^2\dot{\gamma}\sin(2\theta)(N^2-k^2).$$

This force, which again is a maximum at the chain center, puts the chain in tension when $\theta\dot{\gamma}>0$, since the chain is tilted in the direction of shear, and in compression when $\theta\dot{\gamma}<0$. For the chain to be stable to fracture this hydrodynamically induced force must be smaller than the radial component of the electrostatic interaction

$$F_{\mathrm{sc},r}=\zeta(3)(3\pi a^2\mu_0\dot{\gamma}/8\ \mathrm{Mn})(3\kappa_1\cos^2\theta-\kappa_2).$$

The maximum stable chain number is determined by balancing these forces at the chain center

$$N_{\max}=\begin{cases}\sqrt{\dfrac{\zeta(3)}{8\ \mathrm{Mn}}\,\dfrac{3\kappa_1\cos^2\theta-\kappa_2}{\sin 2\theta}}, & \dot{\gamma}\theta\geqslant 0\\ \infty, & \dot{\gamma}\theta<0.\end{cases} \tag{31}$$

The maximum stable chain length is extremely dependent on chain orientation and strain rate, especially when driven by oscillatory shear. The maximum stable chain length diverges when the chain is aligned with the field, when the instantaneous strain rate is zero, and when the chain is under compression.

If a chain is far from its maximum stable size then its size will adjust by aggregation or fragmentation. We will describe the kinetics of aggregation and fragmentation by the phenomenological formula

$$\frac{dN(t)}{dt}=\frac{k}{N(t)}\left[1-\frac{N(t)^2}{N_{\max}^2(t)}\right], \tag{32}$$

where because induced dipolar forces drive aggregation the rate constant it is useful to write $k=k_0[\zeta(3)\kappa_3\varepsilon_0\varepsilon_c\beta^2E_0^2/8\mu_0]$, where k_0 is a concentration-dependent constant with no implicit field or viscosity dependence. The reasons for this definition of k_0 will become obvious in the following.

This kinetic equation gives very different time dependences for aggregation and fragmentation. When the chain is much smaller than its maximum stable length, slow, power-law aggregation will occur with $N(t)=\sqrt{N(0)^2+2kt}$, in agreement with the root time prediction of See and Doi [32], which they developed for the quiescent fluid. If the chain is much larger than its stable length then fragmentation will occur exponentially quickly according to $N(t)=N(0)e^{-kt/N_{\max}^2}$. Note that the fragmentation rate $k/N_{\max}^2$ is proportional to the strain rate and is *independent* of the electric field and viscosity. Of course, when the chain is at its maximum length no aggregation or fragmentation occurs since $dN(t)/dt=0$. Thus the phenomenological rate equation gives physically reasonable behavior while avoiding the complexities of the Smoluchowski equation.

Equations (30)–(32) now comprise a set of coupled nonlinear equations that can be solved to model the dynamics of chains in shear flow. However, at this point there are four independent parameters in the system: the Mason number Mn, the strain frequency ν and amplitude γ_0 and the rate constant prefactor k_0. A considerable simplification occurs by recognizing that solutions to the kinetic equation are of the form $N(t)=[\zeta(3)\kappa_3\dot{\gamma}/16\nu\ \mathrm{Mn}]^{1/2}n(\nu t)$. If all functions are expressed in terms of the dimensionless time $s=\nu t$ this leads to the reduced damped nonlinear oscillator equations

$$\dot{\theta}+\frac{1}{n^2}\sin2\theta=\dot{\gamma}\cos^2\theta,\quad \dot{n}=\frac{k_0}{n}\left[1-\frac{n^2}{n_{\max}^2}\right],$$
$$n_{\max}=\begin{cases}\sqrt{\dfrac{2}{\dot{\gamma}}\dfrac{3\kappa_1\cos^2\theta-\kappa_2}{\kappa_3\sin2\theta}}, & \dot{\gamma}\theta\geqslant0\\ \infty, & \dot{\gamma}\theta<0.\end{cases} \tag{33}$$

The reduction to a three-parameter (γ_0,k_0,β) model is a result of the particular form of the rate equation we have chosen. The strain amplitude is fixed in the experiment and β can be computed, so this is really a single free parameter model. Finally, it is interesting to note that the chain orientation dynamics $\theta(t)$ is independent of Mason number, although the chain length dynamics $N(t)$ is not.

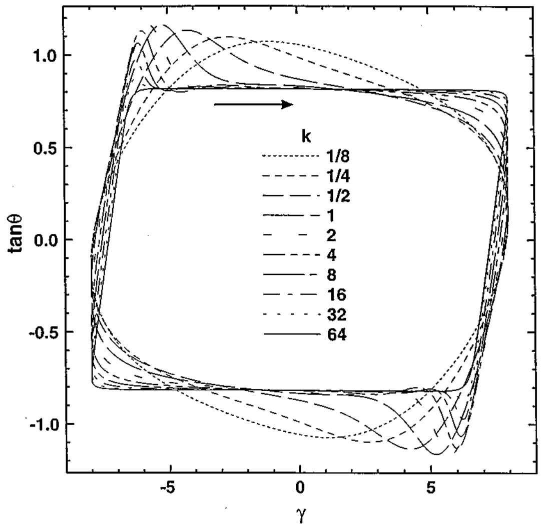

FIG. 27. Lissajous plots change unexpectedly as the rate constant k is varied. For $k=0$ the oscillator reorientation rate ω_d is a simple constant and the remaining nonlinearities are small enough that a nearly elliptical response is observed. For large k Lissajous plots approach a parallelogram, whereas for intermediate-k values retrograde motion is observed.

1. Electrorheology

Before we discuss the behavior of these equations we would like to discuss the predicted rheology. In terms of the volume fraction ϕ of spheres the field-induced contribution to the fluid stress is

$$\sigma=6\mu_0N^2\phi(\dot{\gamma}\cos^2\theta-\dot{\theta})=\tfrac{9}{8}\varepsilon_0\varepsilon_c\beta^2E_0^2\phi\zeta(3)\kappa_3\sin2\theta. \tag{34}$$

From the right-hand side of this equation it is clear that the fluid stress increases with the chain orientation angle. When $\theta=0$, the chain contribution to the fluid stress is zero and the chain comoves with the fluid so $\dot{\gamma}\cos^2\theta=\dot{\theta}$. Because Eq. (33) shows that the dynamics of chain orientation is independent of electric field and shear frequency, we conclude from Eq. (34) that the stress scales purely as the square of the electric field.

2. Numerical results

We can now compare the predictions of this model with our experimental results. For this purpose we have used the dielectric constant of 13.5 for 4-methylcyclohexanol and 4 for silica, giving a negative value of β. For small strains the response is sinusoidal, as expected, but for large strains (Figs. 27 and 28) Lissajous plots are nonelliptical and dependent on the rate constant k. For $k=0$ the oscillator reorientation rate ω_a is a simple constant and the remaining nonlinearities in Eq. (30) are small enough that a nearly elliptical response is observed. As k increases, the chains fragment and aggregate to achieve mechanical stability while trying to maximize their length and Lissajous plots approach a parallelogram. The instantaneous response limit (large k) of the local-field-corrected model is in good agreement with the data in Fig. 22. This agreement is much better than the bare model because of the reduced orientation angle. Finally, for

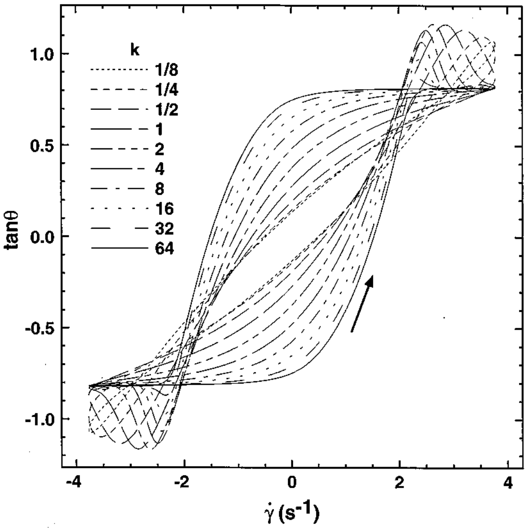

FIG. 28. The orientational dynamics shown in Fig. 27 are plotted as functions of the strain rate. As the rate constant k increases, the nonlinear dynamics becomes more pronounced.

intermediate values of k an interesting crossover is observed wherein humps appear in the Lissajous plots. This hump is commonly observed in our data at low fields, as illustrated in Figs. 23 and 24.

The nonlinear behavior of this system is also shown as a Lissajous plot of the chain angular velocity versus the chain angle (Fig. 27). Again, the detailed shape of the theory is somewhat different from the data, but the overall agreement is quite good.

The chain orientation dynamics is a somewhat indirect test of the kinetic chain model since it is conceivable that one could construct another set of equations that gives the same overall behavior. However, the nonlinear behavior of this model is ultimately driven by the fragmentation and aggregation phenomena that occur during each shear cycle. The dynamics of fragmentation, which occurs at twice the oscillation frequency, is shown in Fig. 29. Chain aggregation is very pronounced just as the electrode is about to return to zero angle, with chains reaching a maximum size just after the maximum strain. During this time interval the chain is more or less comoving with the flow. Fragmentation occurs much before the electrode returns to zero angle because the chain is nearly 90° ahead of the strain and thus is already at its maximum tilt angle in the opposite direction. The power-law aggregation and exponential fragmentation leads to an obvious asymmetry in the chain size peaks.

Large aggregates cause intense light scattering, so to measure the chain size we determined the wedge integrated maximum intensity $I_{\max}$ (as opposed to the peak position $\theta_{\max}$) for each scattering image. The peak intensity is plotted against time in Fig. 30 and against chain orientation in Fig. 31. There is a very close correspondence between these data and the prediction (Fig. 29) of the kinetic chain model. The peak position relative to the applied strain is about right and even the peak asymmetry, due to slow aggregation and fast fragmentation, can be seen. Moreover, this pattern was observed in all of the data sets, except those taken at a strain amplitude of 0.25, despite the tremendous variations in Lissajous plots of the orientational dynamics.

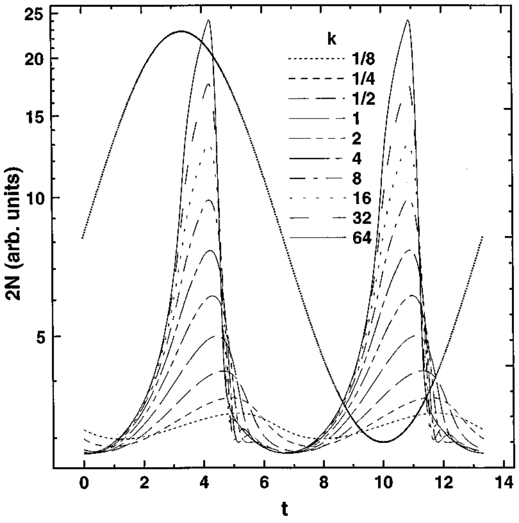

FIG. 29. The chain length varies considerably during the strain cycle due to fragmentation at large chain angles and aggregation at small angles. The asymmetry of the peaks is due to the power-law aggregation kinetics being slower than the exponential fragmentation. The sinusoid is the strain.

D. Phase bifurcation

The oscillatory shear measurements we have reported thus far have been at low to moderate fields. When the voltage is turned up to greater than about 1.0 kV we found that the scattering lobes split into two pairs. Direct observation indicated that the phase and amplitude of motion of the two pairs differed. After digitizing the scattering data we found that, due to the finite lobe width, the pairs of lobes could be distinguished from each other only when the strain amplitude

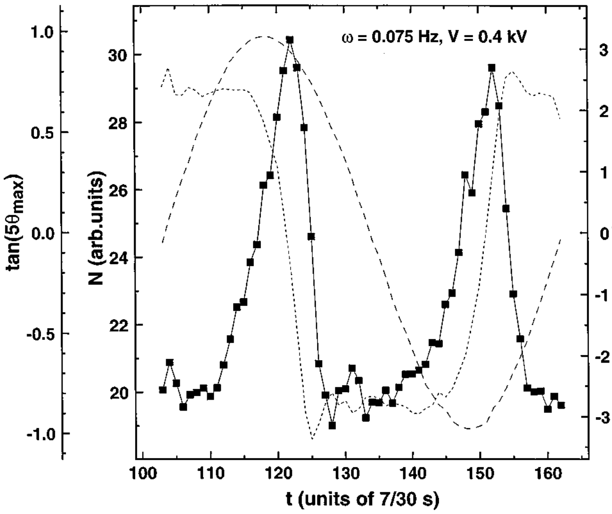

FIG. 30. When the maximum intensity (solid line, plotted against the first left axis) is plotted against time, the resulting curve is very similar to the chain length fluctuations of Fig. 29. The strain is the sinusoid (plotted against the right axis) and the chain orientation is the small dashed line plotted against the second left axis. These data, taken at a strain amplitude of 3.2, are representative of data taken at strain amplitudes down to 0.5. Intensity fluctuations are small when the strain amplitude is 0.25.

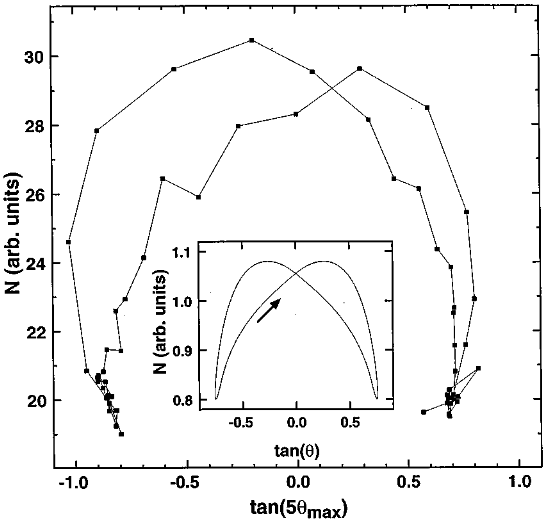

FIG. 31. The data of Fig. 30 are used to make a Lissajous plot of chain size versus orientation. The inset is a typical computed Lissajous plot of chain length versus orientation for the kinetic chain model. The asymmetry in the data is exaggerated in this representation.

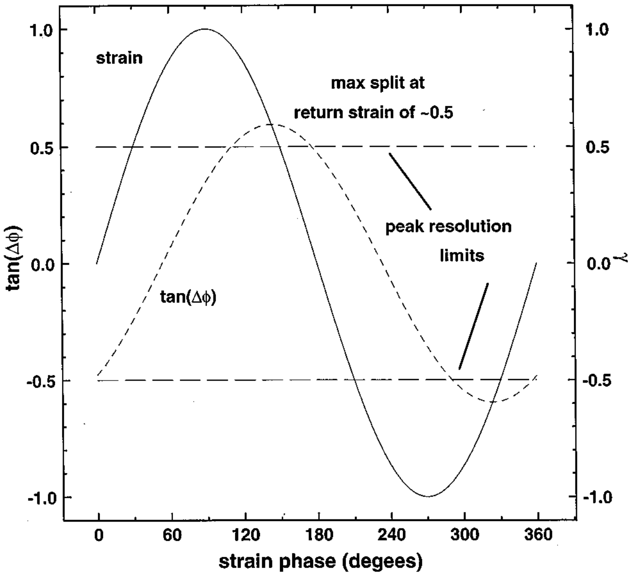

FIG. 33. The difference between the tilt angle of scattering lobes that are in phase and out of phase with the applied strain reaches a maximum when the strain is at half maximum on the return stroke, i.e., 150° and 330°.

is roughly half maximum on the return stroke (i.e., at strain phase angles of about 150° and 330°, where 0° is defined as the zero strain amplitude on the positive outgoing stroke). The resolved peaks are shown in Fig. 32. We attribute this phase bifurcation to the onset of a shear slip instability [33], with one population of chains growing out from each electrode and a second population of free droplets in a central high shear rate slip zone. If a shear slip instability is indeed the cause of phase bifurcation, then the free droplets in the shear slip zone should be subject to a large hydrodynamic torque and should thus be nearly in phase with the strain, whereas the bound chains should feel little hydrodynamic torque and should be out of phase with the strain.

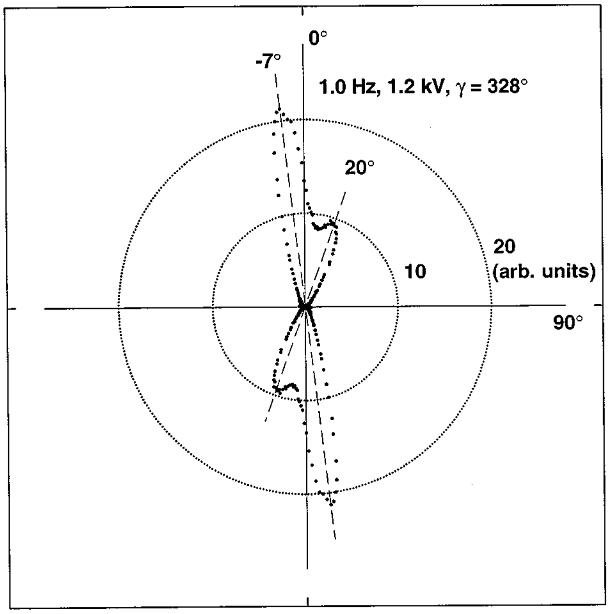

FIG. 32. As the voltage is increased the scattering pattern bifurcates into two pairs of lobes that oscillate at about 90° out of phase with one another. When the applied strain is at half maximum on the return stroke (i.e., at 150° and 330°) the two lobes can easily be resolved, as shown here. We attribute this phase bifurcation to the onset of a shear slip instability, with free droplets in the shear zone and bound chains attached to the electrodes. Direct microscopy studies on this fluid support this conclusion.

Because the scattering lobes cannot be resolved throughout most of the strain cycle, it is not possible for us to directly determine the phase of each component. Instead, we generated the response functions $\theta_{\mathrm{in}}(t)$ for in phase and $\theta_{\mathrm{out}}(t)$ for out of phase oscillators and plotted the difference $\Delta\theta(t) = \theta_{\mathrm{out}}(t) - \theta_{\mathrm{in}}(t)$ between these functions in Fig. 33. It is apparent that the scattering lobes will be resolved when $\Delta\theta > \sigma_\theta$, where σ_θ is the width of the lobes. Thus, when $\Delta\theta$ is a maximum we have the best chance of resolving the peaks, and this does indeed occur at the half maximum strain on the return stroke. This is strong evidence in support of two structural components (free droplets and bound chains) that arise due to the formation of a shear slip zone.

VI. CONCLUSIONS

We have presented light-scattering studies of an electrorheological fluid in the quiescent state, steady shear, and oscillatory shear. Studies of the coarsening of the quiescent fluid after a field quench show that the growth of structure in many ways mimics the spinodal decomposition of a binary fluid. The analogy with spinodal decomposition is strong; a peak appears in the structure factor, the high-q shoulder of which conforms to Porod's law of scattering from sharp interfaces while the low-q shoulder increases as q^2, and the domain size increases as a power of time. However, close examination reveals that the domain growth exponent is smaller than the 1/3 value predicted for spinodal decomposition in a system with a conserved order parameter. We find the kinetics data are better described by a thermal model of hierarchical clustering of columns into successively larger columns. The interaction between columns is presumed to arise from one-dimensional charge-density fluctuations in the columns that persist long enough to allow columns to collide. This model also gives a good account of the increase in the growth kinetics with applied voltage.

Studies of an ER fluid in steady shear show that the structure reaches a steady state wherein droplets are rotated in the direction of fluid vorticity at some angle θ relative to the applied electric field. This angle is found to increase as the cube root of the shear rate, in agreement with a model we originally proposed for the shear thinning viscosity. In this model the equation of motion of elliptical droplets is found by balancing the hydrodynamic and electrostatic torques. The droplets reach their free-energy minimum by fragmenting to align with the electric field until exposing more surface finally becomes too energetically costly.

Our studies of ER fluids in oscillatory shear demonstrate that the chain dynamics, and thus the electrorheology, is nonlinear. We have described a simple kinetic chain model of the dynamics that describes the approach of a chain to its maximum stable size by a kinetic equation. Much of our experimental data can be described by taking the instantaneous approach to stability; however, at low fields strong nonlinearities suggest that the approach to stability is slow compared to the shear period. This model is then used to compute the nonlinear rheology of an ER fluid and it is concluded that light scattering is an indirect probe of stress.

At high voltages we observe a phase bifurcation in the scattering pattern that we attribute to the onset of a shear slip zone. Free droplets in the shear slip zone oscillate out of phase with bound chains attached to the electrodes.

ACKNOWLEDGMENTS

The work of J.E.M. and J.O. was performed at Sandia National Laboratories and was supported by the U.S. Department of Energy under Contract No. DE-AC04-94AL85000.

[1] H. Block and J. P. Kelly, J. Phys. D **21**, 1661 (1988).

[2] A. P. Gast and C. F. Zukoski, Adv. Colloid Interface Sci. **30**, 153 (1989).

[3] R. A. Anderson, in *Proceedings of the International Conference on Electrorheological Fluids: Mechanism, Properties, Structure, Technology and Applications*, edited by R. Tao (World Scientific, Singapore, 1992).

[4] R. A. Anderson, Langmuir **10**, 2917 (1994).

[5] L. C. Davis, Appl. Phys. Lett. **60**, 319 (1992).

[6] J. E. Martin, J. Odinek, and T. C. Halsey, Phys. Rev. Lett. **69**, 1524 (1992).

[7] J. E. Martin, J. Odinek, and T. C. Halsey, Phys. Rev. E **50**, 3263 (1994).

[8] J. E. Martin and J. Odinek, Phys. Rev. Lett. **75**, 2827 (1995).

[9] J. M. Ginder, Phys. Rev. E **47**, 3418 (1993).

[10] K. L. Smith and G. Fuller, J. Colloid Interface Sci. **155**, 183 (1993).

[11] D. Adolf and T. Garino, Langmuir **11**, 307 (1995); D. Adolf, T. Garino, and B. Hance, *ibid.* **11**, 313 (1995).

[12] T. C. Halsey and W. Toor, J. Stat. Phys. **61**, 1257 (1990).

[13] T. C. Halsey and W. Toor, Phys. Rev. Lett. **65**, 2820 (1990).

[14] R. Tao and J. M. Sun, Phys. Rev. Lett. **67**, 398 (1991).

[15] T. Chen, R. N. Ritter, and R. Tao, Phys. Rev. Lett. **68**, 2555 (1992).

[16] T. C. Halsey, J. E. Martin, and D. Adolf, Phys. Rev. Lett. **68**, 1519 (1992).

[17] J. E. Martin and R. A. Anderson, J. Chem. Phys. **104**, 4814 (1996).

[18] J. E. Martin, D. Adolf, and T. C. Halsey, J. Colloid Interface Sci. **167**, 437 (1994).

[19] T. C. B. McLeish, T. Jordan, and M. T. Shaw, J. Rheol. **35**, 427 (1991).

[20] J. A. Powell, J. Rheol. **39**, 1075 (1995).

[21] A. P. Philipse and A. Vrij, J. Colloid Interface Sci. **128**, 121 (1987).

[22] L. Landau and E. M. Lifshitz, *Statistical Physics*, 2nd ed. (Pergamon, Oxford, 1984).

[23] G. K. Batchelor, *Introduction to Fluid Dynamics* (Cambridge University Press, New York, 1967).

[24] W. B. Russel, D. A. Saville, and W. R. Schowalter, *Colloidal Dispersions* (Cambridge University Press, New York, 1989), Chap. 2.

[25] D. R. Nelson, Physica A **177**, 220 (1991); D. R. Nelson and H. S. Seung, Phys. Rev. B **39**, 9153 (1989).

[26] R. D. Kamien and D. R. Nelson, J. Stat. Phys. **71**, 23 (1993).

[27] J. D. Gunton and M. Droz, *Introduction to the Theory of Metastable and Unstable States* (Springer-Verlag, Berlin, 1983).

[28] J. S. Langer, M. Bar-on, and H. D. Miller, Phys. Rev. A **11**, 1417 (1975).

[29] G. B. Jeffry, Proc. R. Soc. London, Ser. A **102**, 161 (1922).

[30] L. Landau and E. M. Lifshitz, *Electrodynamics of Continuous Media*, 2nd ed. (Pergamon, Oxford, 1984), Chaps. 1 and 2.

[31] W. Toor and T. C. Halsey, Phys. Rev. A **45**, 8617 (1992).

[32] H. See and M. Doi, J. Phys. Soc. Jpn. **60**, 2778 (1991).

[33] D. F. Klingenberg and C. F. Zukoski, Langmuir **6**, 15 (1990).